AMERICAN METEOROLOGICAL SOCIETY

Meteorological Monographs

EARLY ONLINE RELEASE

The DOI for this manuscript is doi: 10.1175/AMSMONOGRAPHS-D-16-0005.1

On the Lifecycle of Individual Contrails and Contrail Cirrus

ULRICH SCHUMANN*,

Deutsches Zentrum für Luft- und Raumfahrt, Institut für Physik der Atmosphäre, Oberpfaffenhofen, Germany

ANDREW J. HEYMSFIELD,

National Center for Atmospheric Research, Boulder, Colorado, USA

For AMS Monography "Ice Formation and Evolution in Clouds and Precipitation: Measurement and Modeling Challenges."

Volume Organizers: Darrel Baumgardner, Greg McFarquhar and Andrew Heymsfield.

Revised Version of June 2016.

*) Corresponding author. Email: ulrich.schumann@dlr.de

ABSTRACT

The lifecycle of individual (initially line-shaped) contrails behind aircraft and of contrail cirrus (aged contrails mixed with other ice clouds) is described. The full contrail lifecycle is covered, from ice formation for given water, heat and particulate emissions, changes in the jet, wake and dispersion phases, until final sublimation or sedimentation. Contrail properties are deduced from various in-situ, remote sensing and model studies. Aerodynamically induced contrails and distrails are explained briefly. Contrails form both in clear air and inside cirrus. Young contrails consume most of the ambient ice supersaturation. Optical properties of contrails are age and humidity dependent. Contrail occurrence and radiative forcing depends on the ambient Earth-atmosphere conditions. Contrail cirrus seems to be optically thicker than assessed previously and may not only increase cirrus coverage but also thicken existing cirrus. Some observational constraints for contrail cirrus occurrence and radiative forcing are derived. Key parameters controlling contrail properties, besides aircraft and fuel properties, ambient pressure, temperature and humidity, are the number of ice particles per flight distance surviving the wake vortex phase, the contrail depth, and particle sedimentation, wind shear, turbulence and vertical motions controlling contrail dispersion. The climate impact of contrails depends among others on the ratio of shortwave to longwave radiative forcing (RF) and on the efficacy with which contrail RF contributes to surface warming. Several open issues are identified, including re-nucleation from residuals of sublimated contrail ice particles.

1. Introduction

Contrails (condensation trails) form behind aircraft as line-shaped cirrus clouds, with high concentrations of small ice particles compared to other cirrus, see Figure 1. Contrails may form as "exhaust contrails" from water and particles emitted by the aircraft engines (Schumann 1996) or as "aerodynamic contrails" forming because of adiabatic cooling near curved surfaces of the aircraft (Gierens et al. 2009; Kärcher et al. 2009). Distrails (dissipation trails) and aircraft-induced cloud holes may also form (Heymsfield et al. 2011). Contrails are mostly short-lived but may persist for many hours when forming in ice supersaturated air (Minnis et al. 1998). Individual contrails deform with time, often merge with other contrails and cirrus and eventually form "contrail cirrus" (Schumann 2002). Contrail cirrus can be distinguished from other cirrus only when traced back to the formation process (Graf et al. 2012). Early studies discussed the visibility and detection aspects of contrails (aufm Kampe 1943; Brewer 1946; Appleman 1953; Ryan et al. 2011), and these studies contributed to the detection of ice supersaturation, contrail persistence, the dryness of the stratosphere, the Brewer-Dobson circulation (Brewer 2000), and hollow ice particles (Weickmann 1945). The climate impact got more attention later (IPCC 1999). The mean radiative forcing from contrails is likely positive, possibly contributing to global warming (Boucher et al. 2013). In contrast to many other climate effects discussed for aviation, contrail cirrus is observable, see Fig. 1f. This review summarizes the present understanding of contrail cirrus and identifies some open questions. The insight gained may be of relevance for cirrus research, contrail climate assessment and mitigation (including optimized aircraft and engines, changed routing, and alternative fuels), not discussed here (Fuglestvedt et al. 2010; Lee et al. 2010; Grewe et al. 2014a; Brasseur et al. 2016). The paper describes first the formation and properties of "individual contrails". This term is used instead of "line-shaped contrails" because it is not clear when a line-shaped contrail ends. The second part describes contrail cirrus.

2. Individual contrails

2. 1 Mean contrail properties

Since contrails start as line-shaped clouds, different from most other cirrus clouds, special integral properties are used. Just as other cirrus particles, each contrail particle has an individual mass m_i, projected particle cross-section area A_i, habit, and orientation (see list of symbols). These properties plus the phase, composition, temperature and wavelength determine the optical extinction efficiency $Q_{ext,\,i}$ and other microphysical and optical properties of each particle (Hansen and Travis 1974). Integral properties peculiar to contrails are the geometrical cross-section area A_c, and the total crystal number N_{ice}, total extinction EA, and total ice mass I per flight distance,

$$N_{ice} = \sum n_i = A_c n_{ice} \,, \tag{1}$$

$$EA = \sum n_i Q_{ext,i} A_i = Q_{ext} N_{ice} \pi r_{area}^2 = A_c \varepsilon = \tau W \,, \tag{2}$$

$$I = \sum n_i m_i = (4\pi/3)\rho_{ice} N_{ice} r_{vol}^3 = IWC\, A_c \tag{3}$$

Here, the volume-mean ice particle concentration n_{ice}, extinction ε, and ice water content IWC occur, with mean extinction efficiency Q_{ext} and ice-bulk density ρ_{ice}, besides optical depth τ and contrail width W. The above equations also define the volume and area-mean radius of the contrail particles, r_{vol} and r_{area}. By tradition, the definitions are set up so that they equal the geometrical radius in the idealized case of monodisperse spherical particles (Hansen and Travis 1974). The effective radius r_{eff} is defined by the ratio of mean particle volume to cross-section area, $r_{eff} = 3\, I\, Q_{ext}/(4\, \rho_{ice}\, EA)$. Again the factor (3/4) enters for consistency with a hypothetical sphere radius. By definition, $r_{vol}/r_{eff} = r_{area}^2/r_{vol}^2$. The ratio $C = r_{vol}/r_{eff}$ depends on ice particles sizes and habits, and needs to be determined empirically; $C \leq 1$ if the ice particles

were spherical. Measured data collected for contrails show that $C \approx 0.7 \pm 0.3$ varies during the lifetime of the contrails and depends on ambient humidity (Schumann et al. 2011).

The aircraft wake evolution is traditionally divided into the jet, vortex, and dispersion regimes (Hoshizaki et al. 1975). After a roll-up phase (Misaka et al. 2015) overlapping with the jet regime, the vortex regime exhibits two phases: a first phase of a coherent counter-rotating vortex pair and a second phase with rapid hydrodynamic vortex breakup and subsequent turbulent dissipation (Gerz and Holzäpfel 1999; Paoli and Shariff 2016).

2.2 Formation of exhaust contrails

2.2.1 Formation conditions

Exhaust contrails form during the jet phase because of engine emissions of water and particles (mainly soot, i.e., impure carbon particles resulting from incomplete combustion of hydrocarbon fuels (Bond et al. 2013; Petzold et al. 2013)) acting as cloud condensation nuclei (CCN). The emissions depend on fuel mass flow m_F per flight distance (all-engine contribution) and on emission indices for exhaust species (gaseous or particulate, EI and PEI; mass and number of emitted species per mass of fuel burned). A fraction $\eta = F/(Q\, m_F)$ of the specific combustion energy Q is used to propel the aircraft (depending on m_F and thrust F), so that the fraction $(1-\eta)$ of Q appears in the young exhaust jet plume, partly in form of kinetic energy of the jets (Schumann 1996). The remainder heats the aircraft wake later, when all motions induced by the aircraft are dissipated. η is known as ”overall propulsion efficiency” in engine technology (IPCC 1999). Contrails form when the exhaust gases exceed liquid saturation at least for a short time. Humidity (measured by partial vapor pressure) and heat (measured by temperature) in the exhaust plume decrease during mixing of the warm and humid exhaust gases with cool ambient air at about the same rate, along a straight mixing line in Fig. 2a. Relative humidity is the ratio of the partial pressure of water vapor in the exhaust relative to the saturation vapor pressure for given temperature. From the Clausius-Clapeyron

equation, the saturation pressure follows a curve in this figure. Therefore, relative humidity is higher inside the plume than at engine exit and in ambient air. Maximum potential supersaturation is reached when the plume temperatures reaches T_{LM} (LM for liquid maximum). The plume humidity exceeds liquid saturation at least briefly when the ambient air temperature T is below a threshold temperature T_{LC} (LC for liquid critical). T_{LC} depends on ambient relative humidity RH (for liquid saturation) and a parameter G,

$$T < T_{LC} = T_{LM} - \frac{p_{sat}(T_{LM}) - RH\, p_{sat}(T_{LC})}{G},\ \frac{dp_{sat}(T_{LM})}{dT} = G,\ G = \frac{M_{air} c_p p EI_{H2O}}{M_{H2O} Q(1-\eta)}, \quad (4)$$

with saturation pressure $p_{sat}(T)$ over liquid water. From these equations, $T_{LM}(G)$ and $T_{LC}(G, RH)$ can be determined by Newton iteration or from approximate solutions (Schumann 2012). The parameter G covers the dependency of the threshold on ambient pressure p, and EI_{H2O}, Q, and η, defined above, and the specific heat capacity c_p of air, and molar masses M_{H2O} and M_{air} of water and air. This Schmidt-Appleman criterion (SAC) (Schumann 1996) does not consider phase changes and the process of ice production. It assumes quick conversion of kinetic energy from the engine jet into internal energy, and simultaneous mixing of heat, water vapor, and aerosols between the exhaust jet and cloud free ambient air. Within the accuracy of temperature and humidity measurements, the SAC has been verified experimentally (Busen and Schumann 1995; Schumann et al. 1996; Jensen et al. 1998b; Schumann et al. 2000). The measurements confirmed earlier findings that ice saturation is insufficient for formation of visible contrails. Fig. 2b-f shows probabilities of contrail formation properties for the global air traffic of 2006 and meteorology from the European Center for Medium-Range Weather Forecasts (ECMWF). The plots show the frequency of flight conditions (p, T, η, RHi), in relation to threshold conditions. Potentially, without phase changes, 90% of the contrails experience liquid supersaturation (RH_{LM}-1) higher than 5% (up to 230% for low T), mainly near plume temperatures of 230 K for ambient temperatures near 220 K.

136 *2.2.2 Contrail ice formation*

137 For conventional jet fuels and engines, contrail ice particles are frozen water droplets
138 containing some soot or other CCN material (Kärcher et al. 1996; Wong and Miake-Lye
139 2010). Because of potentially high liquid supersaturation, liquid droplets form even on less
140 hygroscopic CCN in the young contrail (Koehler et al. 2009). This is supported by particle
141 refractive index measurements in young contrails suggesting internal mixtures of soot in
142 contrail ice particles (Kuhn et al. 1998). A significant reduction of interstitial non-volatile
143 particles has been observed when contrails form, indicating that exhaust soot indeed
144 participates in ice formation (Schröder et al. 1998). Besides soot, volatile aerosol forming in
145 the engine exhaust plume may also contribute to ice nucleation, in particular at low ambient
146 temperatures and for low soot particle emissions ($< 10^{14}$ kg^{-1}) and low ambient temperatures
147 (< 213 K) (Kärcher and Yu 2009; Wong and Miake-Lye 2010). High concentrations of
148 volatile aerosol have been observed (Fahey et al. 1995). The effect of fuel sulfur content is
149 smaller than expected initially (Schumann et al. 1996; Jurkat et al. 2011).

150 For ~10 % of all contrails, the ambient temperature is only 1 K below the threshold
151 temperature. Here, details of the CCN become important (Kärcher et al. 2015). Ice particles
152 form either by homogeneous freezing of the liquid droplets (not involving ice nuclei) or
153 heterogeneously by ice nuclei (Wong and Miake-Lye 2010). The fraction f_c of soot particles
154 forming droplets decreases with soot loading because of the increased competition for the
155 vapor available for condensation (Kärcher et al. 1996; Paoli et al. 2013). For alternative fuels,
156 with different aerosol and aerosol precursor emissions, ice may form by freezing of water
157 droplets forming on soot (possibly heterogeneously) for high soot concentrations and from
158 volatile material (homogeneously) for less soot (Rojo et al. 2015).

159 The number N_{ice} of ice particles per flight distance forming in the young contrail depends
160 also on the time available for condensation and for ice formation. Without freezing, the

161 contrail particles would soon evaporate even in ice-supersaturated but liquid-subsaturated air.
162 The liquid droplets freeze quickly after formation because of low temperature and high
163 relative humidity in the contrail. Liquid saturation may persist more than 10 s along the plume
164 axis but < 0.1 s at the outer edge of the exhaust plume. Faint contrails become visible to
165 passengers already close to the engine exit for low temperature, see Fig. 1d, and about a wing
166 span after engines under threshold conditions (Busen and Schumann 1995). In the interior of
167 the well-mixed plume, condensation starts many wing spans behind the engine (Schumann et
168 al. 1996; Paoli and Shariff 2016). Outside the plume center, mixing proceeds far quicker,
169 leaving less time for condensing water during liquid supersaturation. Ice particles at the outer
170 edge of contrails experience higher relative humidity and less competition for the available
171 moisture than in the center, thereby getting larger than in the contrail interior, as observed
172 (Petzold et al. 1997; Heymsfield et al. 1998).

173 *2.2.3 Mixing and plume dilution*

174 Mixing of the exhaust jet plume depends on interaction between the jet and the wake
175 vortices in the roll-up phase (Khou et al. 2015), with similar characteristic timescales of
176 mixing and condensation (Wong and Miake-Lye 2010; Paoli et al. 2013). The wide range of
177 time scales may be important for contrail formation from alternative fuels.

178 Mixing can be expressed in terms of a dilution ratio N_{dil} (Schumann et al. 1998). Here,
179 N_{dil} is the mass of air inside the plume per mass of fuel burned, both per flight distance. This
180 definition avoids any dependence on air-fuel ratio in the engine which arises if dilution is
181 defined relative to engine exhaust mass flow. Measurements have shown that the dilution of
182 tracers near the plume center follows approximately

183 $$N_{dil} \approx 7000(t/t_0)^{0.8}, \qquad (5)$$

where t_0= 1 s. This result is a bit surprising because it is independent of aircraft and atmosphere scales, but has been confirmed by various measurements, and applied successfully for estimates of aircraft exhaust concentrations and plume ages (Schäuble et al. 2009; Rojo et al. 2015).

2.2.4 Soot emissions

Since other emissions scale with fuel consumption m_F per flight distance and with an emission index, it makes sense to define an apparent particle emission index PEI_{ice} such that $N_{ice} = PEI_{ice}\, m_F$. If each ice particle would share the same amount of exhaust water, in ice-saturated ambient air, and after cooling to ambient temperature, then the volume mean radius would be

$$r_{vol} \approx \left[3EI_{H2O}/\left(4\pi\rho_{ice}PEI_{ice}\right)\right]^{1/3}, \quad (6)$$

implying $r_{vol} \approx 0.67$ μm for EI_{H2O}=1.24 and PEI_{ice} =10^{15} kg^{-1}, with $\rho_{ice} \approx 917$ kg m^{-3} as ice bulk density (if without air bubbles). This simple analysis shows the high importance of PEI_{ice} for contrail properties. Since we expect $PEI_{ice} = f_c\, PEI_{soot}$, we need to know f_c and the soot number emission index.

Soot formation, mainly from fuel aromatics, is fuel, engine and power dependent (Moore et al. 2015). Lower fuel aromatics (naphthalene) content reduces PEI_{soot} (Braun-Unkhoff and Riedel 2015). Modern engines tend to emit less soot than older ones (Lee et al. 2010). The mass m_{soot} of soot particles, relating $EI_{soot}=m_{soot}\, PEI_{soot}$, increases with thrust setting (Timko et al. 2010). The mass-specific soot emission index EI_{soot} is traditionally determined from ground tests (using smoke number measurements), and more recently from ground-based direct measurements (Timko et al. 2010; Boies et al. 2015). EI_{soot} at cruise can be estimated from ground-based measurements and engine parameters (Peck et al. 2013). Stettler et al. (2013) show that current methods deriving aircraft soot mass emissions from smoke number

data may underestimate the mass emissions by about a factor of three, partly because smaller particles contribute little to the smoke number measurement. From the few experimental data points from in-situ measurements behind cruising civil subsonic aircraft, in particular during the former SUCCESS (Anderson et al. 1998) and SULFUR projects (Petzold et al. 1999; Schumann et al. 2002), one finds PEI_{soot} of 0.2 to 10×10^{15} kg^{-1} and $m_{soot} \approx (4\pm2)\times10^{-20}$ kg. More information is required on soot number emissions (PEI_{soot}) and on the fraction f_c of soot acting as CCN for given contrail formation conditions.

2.2.5 Number of ice particles formed

Ice particles and soot particles under cruise conditions are difficult to measure simultaneously. Part of the soot gets scavenged by contrail ice (Schröder et al. 1998), and therefore ice and soot are measured behind aircraft separately in dry or wet plumes (Brock et al. 2000). The mentioned SULFUR project showed that the number of ice particles in young contrails is comparable to the number of soot particles emitted from the engines. PEI_{ice} increases slightly (by factor <2) when fuel sulfur content increases from 6 to 2800 μg/g. The effective PEI_{ice} derived from in-situ contrail ice particle measurements (Schröder et al. 2000) with dilution from Eq. (5) varies between 10^{14} and 10^{15} kg^{-1} (Schumann 2005). During a more recent field experiment "CONCERT" (Voigt et al. 2010), ice particle concentrations were measured in contrails behind various airliners for contrails of a few min age. The derived PEI_{ice} values vary between 0.7 and 7.2×10^{14} kg^{-1}, with the higher values in the secondary wake above the sinking primary wake (Jeßberger et al. 2013). The results were compared with PEI_{soot} values derived from ground measurements for given flight conditions, and it was found that PEI_{ice} is larger than the PEI_{soot} (Schumann et al. 2013a). This suggests that aircraft either emit more soot particles suitable for contrail formation than estimated or that particle losses are less than predicted. The effect of alternative fuels on particle emissions and the formation of contrails is investigated since May 2014 within ACCESS II and ECLIF projects (B.

Anderson and H. Schlager, AGU 2015). In summary, $N_{ice,0}$ in the young contrail can be estimated from the soot emissions and the fuel consumption per unit flight distance,

$$N_{ice,0} = PEI_{ice} m_F = f_c PEI_{soot} m_F \,. \quad (7)$$

2.3 Aerodynamic contrails, distrails and cloud holes

Aerodynamic contrails show nicely colored iridescent line clouds (Fig. 1b). Contrail iridescence was observed for contrails early (Sassen 1979). Aerodynamic contrails form from intense adiabatic cooling in the airflow over aircraft wings (Gierens et al. 2009). The colors in the aerodynamic contrail are explained by the rapid growth of nearly monodisperse particles, which are visible when observed close to the sun (Kärcher et al. 2009). Only recently it was shown that most of the visible particles form from homogeneous droplet nucleation (Jansen and Heymsfield 2015). The meteorological conditions for aerodynamic contrail formation have been examined in a case study and globally (Gierens et al. 2011; Gierens and Dilger 2013). Visible aerodynamic contrails occur in an altitude range between roughly 540 and 250 hPa, preferentially at temperatures between -20°C and -50°C, and for RH> 80% (Jansen and Heymsfield 2015). The number of ice particles formed in aerodynamic contrails is not well known, but likely smaller than for exhaust contrails (Kärcher et al. 2009). Often exhaust and aerodynamic contrails form simultaneously (see Fig. 1a and b). Aerodynamically induced ice particles may cause inadvertent seeding of ice in supercooled clouds. This explains observed aircraft-induced holes in clouds, at temperatures between -10 to -20°C (see Fig. 1c). These holes may contribute to snow precipitation near airports (Heymsfield et al. 2011). Distrails (dissipation trails) are visible occasionally from ground and in satellite images as linear gaps in clouds (Duda and Minnis 2002). Distrails may result from exhaust or from mixing induced by aircraft (Scorer and Davenport 1970). For nice distrail photos and historical remarks, see Pedgley (2008).

2.4 Contrail wake vortex phase

Wake vortices depend on aircraft properties including aircraft wing span s, mass M, true air speed V, and on atmosphere parameters, such as air density ρ, Brunt-Väisälä frequency N_{BV}, turbulence dissipation rate ε_t, and gravity g, which together define wake vortex scales:

$$b_0 = \frac{\pi}{4} s,\ \Gamma_0 = \frac{gM}{b_0 \rho V},\ t_0 = \frac{2\pi b_0^2}{\Gamma_0},\ w_0 = \frac{b_0}{t_0},\ N_{BV}^* = N_{BV} t_0,\ \varepsilon_t^* = \frac{(\varepsilon_t b)^{1/3}}{w_0}. \quad (8)$$

Here, b_0 measure the lateral distance between the vortex lines, Γ the integral vortex circulation, and t_0, w_0, N^*_{BV}, and ε_t^* are the related time, velocity, stratification and dissipation scales. The wake vortex forms because of aerodynamics: Lift balances aircraft weight by inducing downward momentum on the air behind the aircraft wing. Lift requires circulation (Kutta-Joukowski theorem). Circulation is the integral of velocity along a line around the wing and equals the integral of the open surface bounded by that line (Stokes theorem). Vorticity departs with the flow from the wing rear edges or the wing tips depending on the lift distribution along the wing (Anderson 2010). Some distance behind the aircraft, a vortex pair forms, which sinks with mean speed w_0 initially, until buoyancy becomes important or until hydrodynamic instabilities have grown sufficiently to cause a sudden breakup into dissipating turbulence. The jet regime ends ~4 to 40 wing spans behind the aircraft, depending on speed, engine number and engine positions, when the exhaust jets and the freshly formed contrails got captured in the wake vortex system (Gerz and Ehret 1996). Depending on this interaction, most of the exhaust gets captured in the primary wake vortex (Greene 1986). Part of the exhaust stays outside and above the sinking primary wake and forms the "secondary wake" (Misaka et al. 2012; Holzäpfel 2014; Paoli and Shariff 2016).

Only a fraction f_s of the ice crystals formed in the jet survives the transition from contrail formation until final decay of the wake vortices (Sussmann and Gierens 1999). Any initial ice supersaturation in the contrail gets reduced rapidly by deposition of the vapor excess on the many ice particles in the jets, before the vortex has descended much and reached its lowest

altitude. The sinking vortex experiences adiabatic heating (Greene 1986), which causes a slight local subsaturation around the ice particles, even sensitive to the Kelvin effect, i.e. a reduction of saturation pressure depending on particle curvature and surface tension (Naiman et al. 2011; Lewellen 2012). As a consequence, the smaller ice particles sublimate and the number of ice particles decreases (Lewellen and Lewellen 2001). The secondary wake contains fewer but larger ice particles and binds more ice water because of quicker mixing with ambient humid air and less heating by adiabatic sinking. At low ambient humidity, the primary wake may sublimate after some time while the secondary wake persists longer (Sussmann and Gierens 2001). The fraction f_s of ice particles surviving the wake vortex depends on temperature and humidity, and on the wake vortex scales, and also on the number and size of ice particles formed in the jet phase. The fraction can be estimated from a parameterization based on several recent large eddy simulation (LES) studies (Unterstrasser 2016). As a consequence, any decrease in particle emissions causes a less than linear decrease in the number of ice particles. It would be important to validate these model results by measurements.

A set of data of individual contrails for ages from seconds to hours is compiled in Fig. 3 from previous in-situ and remote sensing observations and from a recent model study. The data include ice particle concentrations, sizes, ice water content, geometrical depth, width, and optical depth. Integral properties (A_c, N_{ice}, EA, I) are also available (to be reported elsewhere). The observations support the assumption that the number of ice particles in contrails is controlled by the heat, humidity and aerosol in the engine exhaust and the formation process in the jet phase, and decrease thereafter. Artifacts produced by crystal shattering on the inlets of the particle probes can yield measurement errors, in particular when large particles are present (Korolev et al. 2011). Most contrail particles, formed at low ambient temperature, are small and, hence, shattering is likely small (Febvre et al. 2009; Voigt et al. 2011). The data synthesis shows no obvious indication, like exceptionally high ice

particle concentrations, that ice particle shattering at instrument inlets had strong effects on past contrail measurements.

It is generally assumed that residuals from sublimated contrail ice particles do not get reactivated when again entering ice supersaturated air. As noted by Zhou and Penner (2014), soot particles processed in contrails may be better ice nuclei than fresh soot. The residuals may still contain some ice in particle gaps that is not sublimated, and the residuals may be quite large when including aerosol parts from nucleation and scavenging. This topic is of relevance both for contrails and cirrus formation and has not been studied conclusively yet. If such reactivation occurs in contrails, it could explain high survival fractions of ice particles in the vortex regime.

Besides the number of ice particles, the depth D and, to minor degree, the width W of the wake vortex systems are important for the climate effect of contrails. The depth influences the optical depth (Voigt et al. 2011); W and D control volume specific ice concentrations and D together with shear and turbulent mixing are important for subsequent horizontal spreading (Konopka 1995). The plume width during the vortex phase is close to aircraft engine span (Greene 1986) but widens during vortex breakup, e.g. after vortex ring formation, and for strong stratification (Misaka et al. 2012; De Visscher et al. 2013).

A parametrization of the wake vortex descent depth D_w during the two wake vortex decay phases has been derived by Holzäpfel (2003). Recent results suggest larger descent distances than predicted. The contrail depth D_c may be smaller when the primary vortex sublimates and larger when buoyancy causes some lift above the flight level. Figure 4 compares results for D, i.e., wake vortex depth and contrail depth, with various experimental data and LES results. The non-dimensional descent D/b_0 depends on the stratification parameter N_{BV}^* and on turbulence, ε_t^*, see Eq. (8). For low stratification, D depends strongly on ambient disturbances initiating hydrodynamic instabilities. For weak shear, vortex rings

may form, after a time 6 b_0/w_0 (Delisi and Greene 2009). The results differ partly because of different initial disturbances, Reynolds number, and numerical resolution. Deep wake depths, possibly sinking beyond $D/b_0 > 20$, are observed in laboratory experiments and idealized simulations with little stratification, little turbulence, and little wind shear, and wind shear gradient (Delisi and Greene 2009). For high humidity, some of the contrail LES results show larger D. It is not clear how much the age (6 min; reaching into the dispersion phase) contributes to the larger D.

The humidity inside dense contrails decreases to ice saturation shortly after contrail formation. This is a consequence of large products $n_{ice}\ r_{area}$ (size per volume) of ice particle concentrations n_{ice} and ice particle sizes r_{area}, implying small timescales t_{sat} of humidity relaxation to saturation by deposition/ sublimation of water vapor on the ice particles, $t_{sat} \approx (4\pi\ D_{H2O}\ n_{ice}\ r_{area})^{-1}$ (Korolev and Mazin 2003). Here, D_{H2O} is the diffusion coefficient of water vapor in air. Kaufmann et al. (2014) measured humidity inside a contrail which was close to saturation fo**r** $n_{ice} = 117\ cm^{-3}$ and $r_{area} = 0.5\ \mu m$, implying $t_{sat} \approx 23$ s. Here, t_{sat} is smaller than the contrail age (>90 s), in spite of the rather small ice particle sizes, in this case. Hence, RHi inside contrails is mostly well relaxed toward saturation. As visualized in LES (Naiman et al. 2011; Picot et al. 2015), deviations from saturation occur at the contrail boundaries.

The total optical extinction $EA=W\ \tau$ of the contrail near the end of the vortex phase depends on Q_{ext} and $N_{ice}=f_s\ f_c\ PEI_{soot}\ m_F$ and $\pi\ r_{area}^2$, see Eq. (2). The ratio C relates r_{area}^2 with r_{vol}^2. The volume radius r_{vol}, Eq. (3), depends on the third root of the mean particle mass. The mean particle mass depends on the bulk density ρ_{ice} and on the amount of water per ice particle in the contrail, i.e., approximately, on the water emission ($EI_{H2O}\ m_F$) distributed over the cross-section $A_c= N_{dil}\ m_F/\rho$, with air density ρ, and the water uptake from ambient air, for

given ice saturation pressure $p_{ice}(T)$, pressure p, temperature T, relative humidity over ice RHi, and air and water molar masses, so that (Jeßberger et al. 2013),

$$EA = \left[\frac{9\pi}{16\rho_{ice}^2}\right]^{1/3} C Q_{ext} m_F \left[f_s f_c PEI_{soot}\right]^{1/3} \left[EI_{H2O} + \frac{(RHi-1) N_{dil} M_{H2O} p_{ice}(T)}{M_{air} p}\right]^{2/3} . \quad (9)$$

Hence, EA grows linearly with fuel consumption m_F, the third root of the ice particle emission index and the 2/3 power of dilution and supersaturation.

Unexpectedly large (15-20 μm effective diameter) ice particles have been measured in young contrails during CONCERT (Jeßberger et al. 2013). The concentration of crystal with diameters exceeding 10 μm could not be reproduced with models for the measured conditions. It seems that some ice particles start to grow early (e.g. at the outer edge of the young exhaust jet, perhaps on small ambient cirrus particles), consume most of the ice supersaturation, and grow to sizes as measured, but details have not been explained.

In summary, after the wake vortex phase, the contrail contains a number $N_{ice} = f_s f_c PEI_{soot} m_F$ of ice particles, and has depth D, width W, and an ice water content I, mainly determined by the jet and vortex dynamics, and ambient humidity, and Eq. (3) determines corresponding particle sizes.

2.5 Contrail dispersion phase

Contrails in the dispersion phase are far more difficult to explain than in the jet and wake phases. Mixing is no longer controlled by aircraft-induced motions. Instead, the atmosphere, with all its complexity, causes mixing. Initially, mixing is controlled mainly by shear and ambient turbulence. Wind shear is highly variable because of mesoscale horizontal motions. Turbulence at flight levels is difficult to predict for many reasons (Sharman et al. 2012; Paoli et al. 2014). Latent heat effects are small for low temperatures. However radiative heating can contribute to destabilize the cirrus and contrail layers by infrared cooling at cloud tops and

terrestrial warming from below, in addition to heating by absorption of solar radiation (Jensen et al. 1998a; Unterstrasser and Gierens 2010a). The process gets far more complex when ice sedimentation gets important, and contrail particles fall into drier or more humid air below the contrail levels (Bock and Burkhardt 2016). The terminal fall speed of particles depends on their size (Reynolds number) and habit (Heymsfield et al. 2013). By sedimentation, large particles separate from the smaller ones, thinning the upper contrail part. The upper part contains most of the exhaust and may still contain a considerable number of small particles, observable as the "contrail core". Smaller ice particles may sublimate earlier than larger ones, in particular when the Kelvin effect becomes important, causing "in-situ" particle losses (Lewellen et al. 2014). Falling ice particles may aggregate with smaller ice particles causing a reduction of the number of ice particles (Kienast-Sjögren et al. 2013). When the larger particles fall into more humid air, the ice particles grow and fall even more quickly, so that fallstreaks develop and eventually precipitate (Freudenthaler et al. 1995; Atlas et al. 2006; Unterstrasser et al. 2012). Hence, the thickness D_{IS} of the ice supersaturated layer below the contrail influences the life-cycle (Sussmann and Gierens 1999; Lewellen 2014). Finally, one has to consider cirrus-contrail interactions. Contrail and natural cirrus particles, when present, compete for ice supersaturated air and this may have strong effects for growth of existing ice particles and nucleation of additional ice particles. Little is known about potential new contrail ice particle formation during the contrail lifecycle. However, the observations collected in Fig. 3 support the assumption that the number of ice particles in contrails does not increase with contrail age (Spinhirne et al. 1998).

The period of contrail existence of radiative importance may be shorter than the whole lifetime: The region in which contrails form may get covered by natural cirrus after contrail formation. Contrails sedimenting into other clouds may get radiatively shielded by the clouds above the contrail.

One may distinguish between externally and internally limited lifecycles of contrails. Contrails are considered to be limited externally when the changing meteorology limits the lifetime, e.g., by sublimation in subsiding air masses. Contrails are limited internally, when the contrails end by sublimation or sedimentation even for fixed meteorology. For both kinds of contrail cirrus, the energy forcing EF (time integral of local radiative forcing RF' weighted with contrail width (Schumann et al. 2012a)) depends on the lifetime. To first order, the EF of externally limited contrails increases with the square of the lifetime and the third root of the number of contrail ice particles per flight distance. For internally limited contrails, the EF depends even more strongly on N_{ice}.

The ice mass I and optical depth τ of contrails increases as RHi increases (Unterstrasser and Gierens 2010b). But this does not necessarily imply that high RHi gives a high climate impact EF. Contrail particles remain small for low ice supersaturation but may exist for a long time because of low fall speeds. For high humidity, the contrail ice particles get large but sediment quickly, so that EF may get largest for weak but long lasting supersaturation (Lewellen 2014; Schumann et al. 2015).

In-situ measurements of aged contrails are difficult because the pilots can hardly distinguish aged contrails from thin cirrus during flight. Thick contrails were followed for ages up to 40 min (Heymsfield et al. 1998; Schröder et al. 2000; Febvre et al. 2009; Jones et al. 2012) and results are included in Fig. 3. Many aged contrails have been sampled with novel cloud instruments on the new research aircraft HALO during the ML-CIRRUS campaign in 2014 (Voigt et al. 2016). In fact, natural cirrus, totally unaffected by aircraft emissions, is rare over Europe. Contrails were measured for contrail ages of at least 1.8 h. Contrail cores were identified from enhanced NOx emissions, traffic data, and trajectory analysis. These contrail parts were found to have still higher concentrations of relatively small ice particles than ambient cirrus.

Important progress has also been achieved by remote sensing of contrails. More than 3400 contrails have been identified in collocated MODIS-CALIPSO images (Iwabuchi et al. 2012). The data brought important statistics on contrail occurrence in the Northern hemisphere and on altitude, width, depth, and length of contrails, lidar backscatter and depolarization, and optical depth. The thinnest contrails detectable in this manner have optical depth >0.03.

Contrails were identified from MODIS and METEOSAT satellite images with an automatic contrail detection algorithm (ACTA) and traced forward and backward in time in METEOSAT images with 5 min temporal and ~4 km horizontal resolution (Vázquez-Navarro et al. 2015). The study observed 2400 contrails, mainly over the Atlantic and Europe at northern midlatitudes, partly multiple times (with increasing ages) during their lifecycle up to maximum ages (lifetimes) of 19 h, and evaluated their optical depth (see Fig. 5), height, width, shortwave (SW) and longwave (LW) RF', as induced by contrails visible, after some dwell time, to METEOSAT. Fig. 6 depicts the observed ages of contrails detected this way. Mean values retrieved are 1 h age, 130 km length, 8 km width, 11.7 km altitude, 0.34 optical thickness. Local RF' values of order ±20 W m^{-2} and EF values of up to 400 GJ km^{-1} during night and -875 GJ km^{-1} over water during daytime were derived. Many contrails are cooling during day. Figure 7 compares the local RF' values derived from these data with results computed with the Contrail Cirrus Prediction Model (CoCiP) coupled to the climate-aerosol model CAM3+/IMPACT (Schumann et al. 2015). The model computes thick and thin contrails with small RF' values, while the observations see mainly the thicker contrails. Both show positive LW and negative SW local RF' values of order 20 W m^{-2}, about 1000 times larger than the global mean, consistent with previous observations (Khvorostyanov and Sassen 1998; Haywood et al. 2009; Laken et al. 2012).

Much has been learned about the fate of aged contrails during dispersion using LES models. Lewellen (2014) analyzed lifetime-integrated properties from 200 individual contrail LES simulations. Contrails reached lifetimes >40 h, widths >100 km, and ice masses >50 kg m^{-1}. The lifetime-integrated ice crystal surface area per length of flight path $SS \sim \int N_{ice} \pi r_{area}^2 dt$ is used as an approximate metric of contrail climate significance. For constant radiative properties of the ice particles, this integral is related to the energy forcing discussed before. Over much of the parameter space, SS is found to vary approximately with the product of the maximum contrail depth and effective number of ice crystals per flight path. None of the LES studies includes the full variability of ambient meteorology, so that lifetimes are likely overestimated.

The scale-range from single-engine jets to the global scale is too large to be covered by LES. Hence, simplified models are used to bridge the scales. Simplified models may be based on scale analysis (Lewellen 2014). An alternative is to use a Lagrangian contrail model, which follows individual contrail segments, using data from weather predictions or climate models, and to simulate the lifecycle of all individual contrail segments as forming for given traffic routes from the global fleet of aircraft. Such an approach has been implemented in CoCiP (Schumann 2012). As shown in Figures 3 to 7, the range of model results is in general agreement with the available observations.

2.6 Optical properties

The climate impact of contrails depends on the optical properties of ice particles and contrails, i.e., besides size and number, mainly on particle habit and contrail optical depth (Yang et al. 2015). Ice particles are never exactly spherical but may have a near-spherical shape (possibly droxtals (Thuman and Robinson 1954)) just after freezing from liquid droplets, and become more non-spherical in humid air quickly thereafter (Bailey and Hallett 2009). Non-spherical ice particles backscatter solar light more strongly laterally and

backwards than do ice spheres. Ice particles with rough surfaces may scatter more strongly than with smooth surfaces. Hence, the SW RF by contrails is underestimated (the net RF is overestimated) when spherical ice crystals are used to represent contrails (Meerkötter et al. 1999; Markowicz and Witek 2011). Schröder et al. (2000) found near-spherical ice particles of a few μm size in young contrails and non-spherical ones in aged contrails and in thin cirrus from images of replica on coated films. Jones et al. (2012) found small (≈10 μm) plate-like crystals in persistent contrails, while larger particles retained a hexagonal habit. Hexagonal plates were also deduced from optical halo observations in aged contrails (aufm Kampe 1943; Sussmann 1997). Gayet et al. (2012) found a decrease of the asymmetry parameter of contrail particles with contrail age in the wake of an A380 aircraft until 4 min contrail age. Xie et al. (2012) derived a contrail habit parameterization matching lidar-observed contrails (Iwabuchi et al. 2012). Schumann et al. (2011) suggested a size-dependent particle habit mix for contrail cirrus studies by combining droxtal-shape particles for small contrail particles and a parameterization for cirrus (Baum et al. 2005) for large contrail particles.

The cumulative distribution function of optical depth τ (near 550 nm) has a negative skewness, see Fig. 5: A few contrails get thick while most have small τ; some are subvisible, and only the thicker ones are observable (Immler et al. 2008; Kärcher and Burkhardt 2013). Early studies assumed large τ values, based on a few lidar observations (Meerkötter et al. 1999). Some global models suggest large fractions of subvisible contrails and τ mean values of about 0.05 (Ponater 2002; Grewe et al. 2014b). The optical depth of contrails is often large for young contrails because of many ice particles of sufficient size, grown by uptake of ambient humidity in narrow plumes with large depths (Freudenthaler et al. 1996; Voigt et al. 2011). Later, τ may grow in rising air masses with increasing humidity, but generally decreases and approaches zero while the contrails spread laterally and finally sublimate. Ground-based lidar and camera observations (Atlas and Wang 2010) detected 200 thin

contrails (average optical depth of 0.2) but one exceptionally thick contrail ($\tau \approx 2.3$) under very humid conditions. A collection of observed τ data is included in Fig. 3. Contrail cirrus may have 2-3 times larger optical depth than derived for linear contrails (Bedka et al. 2013; Minnis et al. 2013). A global mean optical depth $\tau \approx 0.29$ of contrail cirrus was computed in a global model (Schumann et al. 2015). The relatively thick contrails detected with MODIS/CALIOP (Iwabuchi et al. 2012) and with ACTA from METEOSAT observations (Vázquez-Navarro et al. 2015) have similar optical thickness, mean: 0.25 to 0.35. Hence, the mean optical depth of aged contrails is likely larger than estimated some years ago.

3. Contrail cirrus

3.1 Transition of contrails into contrail cirrus

Eventually, contrails change their morphology depending on the humidity, shear, stratification, waves, turbulence, radiative heating, etc. Individual contrails mix with other contrails and with other cirrus, see Fig. 1g, forming "contrail cirrus" (Liou et al. 1990; Schumann and Wendling 1990). Overlapping contrails produce less total extinction than individual contrails, because of competition for humidity. This competition is nicely illustrated in Fig. 8. Hence, the climate impact increases less than linearly with traffic density (Unterstrasser and Sölch 2012). The transition of an individual contrail into contrail cirrus can be observed for an aircraft flying spirals, as shown for an impressive example in Fig. 9 (Haywood et al. 2009). "Contrail outbreaks" contain many aged and young contrails simultaneously and spread over large areas (Duda et al. 2001).

3.2 Meteorological conditions for contrail occurrence.

Contrail assessments require accurate data on ambient meteorology. The SAC criterion for contrail formation is satisfied only at low enough temperatures. Contrail persistence depends on a humidity threshold. Relative humidity depends on saturation pressure and hence

528 on temperature, and temperature and vertical motions are key determinants for humidity. Also
529 the optical properties and life cycle of contrails depend strongly on meteorological properties,
530 in particular on wind shear, vertical motions, turbulence and ambient cirrus clouds. Even
531 more important, the RF and climate impact depend on all these meteorological parameters and
532 in addition on the albedo and the brightness temperature of the atmosphere without contrails
533 (Schumann et al. 2012a).

534 Great progress has been achieved in numerical weather prediction (NWP) models with
535 proper data assimilation over recent decades (Bauer et al. 2015). Hence, one may assume that
536 temperature can be well predicted. In fact, NWP data have been found to differ from in-situ
537 data at flight levels by less than 0.5 K on average (Dyroff et al. 2015). Such accuracies are
538 more difficult to achieve in climate models, without data assimilation, which often suffer from
539 a cold temperature bias at the tropopause (Marquart et al. 2003; Irvine and Shine 2015; Wu
540 and Pauluis 2015). A cold bias not only increases the apparent relative humidity and the
541 frequency of contrail formation but also increases the computed LW RF of contrails at those
542 temperatures.

543 Until recently, there was some uncertainty whether persistent contrails form only in cloud
544 free supersaturated areas or also inside cirrus (Spichtinger et al. 2005; Burkhardt et al. 2008).
545 Contrail formation in clear sky can be observed often. But contrails also form when the sky is
546 covered, possibly with thin or even subvisible cirrus (Immler et al. 2008). The SAC threshold
547 temperature of contrail formation is slightly higher in cirrus than in clear air (Gierens 2012),
548 because the IWC from cirrus adds some humidity. High ice supersaturation has been
549 measured in-situ outside and inside cirrus (Ovarlez et al. 2000; Jensen et al. 2001; Ovarlez et
550 al. 2002; Comstock et al. 2004). Ice saturation inside cirrus is to be expected for long time
551 scales of return to saturation, i.e., for small mean sizes of ice particles per volume (product

552 r_{area} n_{ice}) (Korolev and Mazin 2003). Contrails embedded in cirrus have been observed and are
553 not much thinner than clear-air contrails (Gayet et al. 1996; Poellot et al. 1999).

554 The frequency of ice supersaturated regions (ISSR) in the upper troposphere is not
555 reliably known. Figure 10 compares mean frequencies of ice supersaturation from a global
556 climatology of ISSR inferred from satellite data, NWP results and a climate model with thin-
557 cloud frequencies from a spaceborne lidar (Lamquin et al. 2012). Climate models tend to
558 overestimate mean ISSR occurrence above the tropopause. Local ISSR are generally shallow,
559 located close to the tropopause with sharp temperature changes (Birner et al. 2002), and form
560 preferably in regions with upwind and divergent airflow (Gierens and Brinkop 2012).
561 ECMWF reanalysis data (ERA interim) imply a mean frequency of 10 % of ISSR at 250 hPa
562 (Irvine and Shine 2015). Airliners fly possibly 15 % of their time in ice supersaturated air
563 masses (Gierens et al. 2012), with about 150 km ±250 km mean length (Gierens and
564 Spichtinger 2000), seasonally variable (Spichtinger and Leschner 2016), consistent with
565 observed contrail occurrences and lengths (Minnis 2003; Iwabuchi et al. 2012). The layers are
566 often 600-800 m thick (extreme values 25 to 3000 m), with 30 % less than 100 m (Dickson et
567 al. 2010).

568 So far, most NWP use one-moment prognostic cloud schemes (only ice mass, not ice
569 number). Some climate models use diagnostic parameterization with assumptions on subgrid
570 scale humidity variability (Burkhardt et al. 2008). Several recent models permit ice
571 supersaturation to occur (Liu et al. 2007; Lohmann et al. 2008), at least in the clear-sky
572 portion of a grid cell (Tompkins et al. 2007). Irvine and Shine (2015) analyzed data from five
573 models used for climate assessments and found that the frequency of exceeding 90% humidity
574 in the annual and global mean at 250 hPa varies from 1 to 19 % (compared to 11 % for ERA-
575 Interim).

576 Accurate routine measurements of humidity values at tropopause levels are demanding.
577 The recently revised MOZAIC data set (Smit et al. 2014) may be used to test previous
578 estimates on ice supersaturation occurrence. Relative humidity depends on saturation
579 conditions; a 0.5 K temperature bias causes 7 % change in RHi at temperature of -60°C.
580 Aircraft humidity measurements have to be corrected for adiabatic heating by air compression
581 in inlets, by 30 K for 240 m/s speed, in addition to sensor deicing heating (Helten et al. 1999).
582 An RHi accuracy of 10 % is not easy to reach, therefore. During research measurement with
583 the DLR Falcon, the sensors often indicated a slightly subsaturated ambient humidity (RHi=
584 95 %) while the contrail that was measured was clearly increasing in IWC to amounts which
585 could be explained only if RHi was near 115% (Gayet et al. 2012; Jeßberger et al. 2013).

586 **3.3 Contrail coverage**

587 Contrail coverage is ill-defined for several reasons. The product of contrail coverage and
588 optical depth controls the radiative forcing (RF) (Lee et al. 2010). For a single contrail
589 segment, this product equals the total extinction, EA. However, difficulties arise when
590 coverage is diagnosed independently of optical depth. Young contrails are distinguished from
591 other cirrus based on their line shape, and this criterion gets uncertain when the contrail gets
592 deformed (Mannstein et al. 1999). Only a small fraction of all linear contrails are detectable
593 from satellites (Mannstein et al. 2010; Minnis et al. 2013). The global contrail coverage was
594 estimated in early studies from regional satellite observations, a potential contrail coverage for
595 given temperature and humidity data, and traffic density (Sausen et al. 1998). Hemispheric
596 observations became available only recently (Duda et al. 2013). Hence, it is not surprising that
597 the coverage of line-shaped contrails derived from satellite data and models varies from about
598 0.06 % to 0.15 % (Rap et al. 2010b; Frömming et al. 2011; Duda et al. 2013). The coverage
599 by contrail cirrus may be far higher than by line-shaped contrails, and factors of order ten
600 (Minnis et al. 2004; Stordal et al. 2005; Burkhardt and Kärcher 2011; Graf et al. 2012) have

been reported; but there is no unique ratio because it depends on the detectability of both, the line-shaped contrails and the total contrail cirrus.

Burkhardt and Kärcher (2011) quantified the amount of contrail cirrus using the global climate model ECHAM CCmod that includes a subgrid-scale cloud class of young contrails. The model captures the life cycle of these man-made clouds and simulates their global coverage, as well as the changes in natural cloudiness that they induce. They computed contrail cirrus coverage of about 0.23 %. Recent attempts to quantify contrail cirrus from MODIS data, allowing for more diffuse contrail contributions, resulted in similar global coverage (Minnis et al. 2013). In CoCiP, the global contrail coverage is computed by superposing the τ contributions from all individual contrails and ambient cirrus and counting fractions of areas in which contrails cause the optical depth of the total cirrus to exceed a certain threshold (Schumann 2012). Contrails not only enhance cloud coverage but also thicken existing cirrus (Minnis et al. 2013; Schumann and Graf 2013) by causing more ice particles, with smaller effective radius, at constant ice water content (Kristensson et al. 2000). This does not exclude that contrails consume humidity and hence reduce natural cirrus (Burkhardt and Kärcher 2011; Unterstrasser and Görsch 2014; Schumann et al. 2015), but the thickening by many additional small ice crystals seems to dominate.

3.4 Contrail-cirrus-soot interactions

Soot from aviation may change cirrus properties also without prior contrail processing, causing "soot cirrus" (Jensen and Toon 1997; Penner et al. 2009; Lee et al. 2010). Modeling studies of the climate impact of aviation soot cirrus remain inconclusive because of the uncertainties in soot abundance and ice-nucleating properties (Koehler et al. 2009; Hendricks et al. 2011; Gettelman and Chen 2013; Zhou and Penner 2014). Enhanced small-sized cirrus particle concentrations with patterns similar to aviation-soot emissions (Ström and Ohlsson 1998; Kristensson et al. 2000) have been observed by in-situ measurements in cirrus in

626 regions with dense air traffic. It is open whether the soot entered the ice during nucleation or
627 later by scavenging.

628 From sublimation of cirrus particles which contain soot (and sulfate) from nucleation or
629 scavenging, soot aggregates may form, possibly with some acid water remainders, which may
630 act as efficient ice nuclei later. On 3 November 2012, a special cirrus pattern was observed
631 near Munich, Germany, as documented with several cameras and ground based lidar and
632 radar. The camera observation method is described in Schumann et al. (2013b). The cirrus
633 was observed between 9.1 and 9.5 km height, was 8-10 km wide, and 35-50 km long. The
634 ambient temperature was below -42°C and the air was ice supersaturated. The cirrus cloud
635 showed a pattern of cirrus with up to 10 parallel line clouds, as if it was formed from aged
636 soot plumes, see Fig. 1e. Back-trajectories show that soot was emitted upstream about 12 h
637 before the event by aircraft. The air ascended and formed cirrus about 4 h before the event.
638 The cirrus lasted for about 1-2 h and then subsided some time and sublimated. About 40 min
639 before the event, the air ascended again and formed the observed cirrus patch. Hence this
640 could be cirrus formed on preactivated aircraft soot. Unfortunately, it cannot be excluded that
641 the same pattern would have formed without air traffic.

642 **3.5 Contrail radiative forcing and efficacy**

643 The RF of contrails is the change in net radiances at top of the atmosphere (TOA) for
644 adding contrails to a given atmosphere (Fuglestvedt et al. 2010). A positive RF causes a mean
645 warming of the atmosphere. A recent study (Dietmüller et al. 2016) confirms that the
646 instantaneous RF does not differ much from the adjusted RF, which is used as global metric
647 for climate change (IPCC 1999). In contrast, RF', the local RF can be defined as the
648 instantaneous change in net incoming radiation for 100 % contrail coverage locally. Contrail
649 RF is composed of a LW and a SW part which depend on traffic and time of day (see Fig. 11).
650 In addition, RF depends on several contrail and Earth–atmosphere-system parameters

651 (Meerkötter et al. 1999). Foremost, RF' of a contrail cirrus layer depends on the optical depth
652 τ (at solar wavelengths), RF' $\approx$ (dRF'/dτ) τ, where the change of RF' with optical depth is of
653 order 100 W/m^2. The dependency of RF on IWP is less systematic than on τ (De Leon et al.
654 2012; Schumann et al. 2012b). The LW RF is positive day and night, and largest for a cold
655 contrail (near the tropopause) over a warm cloud-free Earth surface. The shortwave RF is
656 mostly negative and largest for contrails over dark surfaces (e.g., cloud-free oceans)
657 (Meerkötter et al. 1999). A new parameterized model was developed to compute the contrail
658 RF (Schumann et al. 2012b) for millions of contrail segments efficiently. The model
659 calculates the RF using the TOA radiances for the contrail free atmosphere as input, as
660 available from NWP. The model parameters are fit to accurate calculations with libRadtran
661 (Mayer and Kylling 2005) over a range of conditions. The model and observations show large
662 regional RF' values, see Fig. 7.

663 The contrail RF computed within a global model depends on the representation of the
664 contrails, on the state of the atmosphere, and on the radiation transfer model used. Myhre et
665 al. (2009) defined a useful test of contrail RF computations, also applied by others (Rap et al.
666 2010b; Frömming et al. 2011; Schumann et al. 2012b; Grewe et al. 2014b; Dietmüller et al.
667 2016). The test considers a 1% homogeneous contrail coverage with fixed contrail properties
668 around 10.5-km altitude and optical depth of 0.3. For various atmosphere and radiation
669 transfer models, the comparison revealed net contrail RF values ranging within a factor of
670 two. However, the results vary far more when each model uses its own selection of optical
671 contrail properties. Unfortunately, the papers reporting results on the Myhre test so far missed
672 to document the contrail temperature, Earth albedo, etc., which would be needed to explain
673 RF model differences. The ratio of the absolute values of the SW RF to LW RF varies in these
674 and other studies from 0.2 to 1 (Schumann and Graf 2013). The net RF depends on how far
675 the LW and SW components cancel each other. For fixed LW RF, the net RF is the smaller

676 the larger the absolute SW/LW RF ratio. This uncertainty is of large importance for
677 quantifying contrail net RF (Boucher et al. 2013). Combined observational and model studies
678 are needed to constrain the SW/LW RF ratio better, for contrails and cirrus.

679 The RF by contrails has been computed in a variety of model studies. Burkhardt and
680 Kärcher (2011) compute an RF due to contrail-cirrus of about 31 mWm^{-2}, including -7 mW
681 m^{-2} for reduced natural cirrus because the contrails consume part of the available water. For
682 slightly higher traffic density (year 2006 instead of 2002), a revised version of this model
683 computes a total contrail cirrus RF of 56 mW m^{-2} (submitted paper). Chen and Gettelman
684 (2013) compute smaller contrail cirrus RF values, 13 ±10 mW m^{-2}. Their model assumes far
685 smaller contrail cirrus ages and ice water contents than other models. Schumann and Graf
686 (2013) determined the RF from aviation-induced cloud changes (beyond individual contrails)
687 by combining observations and model results, see Fig. 12. A double peak in the diurnal cycle
688 of cirrus coverage and outgoing LW radiation was detected in the North Atlantic region in
689 correlation with air traffic peaks, one in early morning and one during afternoon. Single
690 images of cirrus derived from METEOSAT with the MeCiDa algorithm (Ewald et al. 2013)
691 often show cirrus patterns indicating aviation induced cirrus changes (for an animation see
692 Graf et al. (2012)). The mean change in outgoing longwave radiation derived from the
693 observations amounts to 600–900 mW m^{-2} for the North Atlantic, a large regional value.
694 CoCiP simulates similar diurnal cycle results for given traffic and meteorological data from
695 ECMWF, but only when increasing humidity by about 10 % in the upper troposphere.
696 Extrapolation with global/regional RF ratios from several models implies a global net RF of
697 about 50 mW m^{-2} (40-80 mW m^{-2}) (Schumann and Graf 2013). These results were used to
698 assess the mean RF and its uncertainty range (IPCC 2013). Recently, CoCiP was run coupled
699 with CAM3+/IMPACT to study the effects of humidity exchanges between contrails and
700 cirrus and the redistribution of humidity in the atmosphere by contrail ice particles (Schumann
701 et al. 2015). The RF values from some of these studies are compiled in Fig. 13. The net RF

results differ less between the simulations than the SW to LW ratio. In all these results, the net RF is positive (implying warming) in the global mean, with an important diurnal cycle. Still, individual contrails often cool, and the local RF' values are far larger than the global mean values (Fig. 7).

The global net RF is often taken as a first-order estimate of the global-mean surface temperature change ΔT_s (Fuglestvedt et al. 2010), $\Delta T_s = \lambda$ RF, with a climate sensitivity parameter λ of 0.8±0.4 K W^{-1} m^2 for a doubling of CO_2 (Stuber et al. 2005). Different forcing mechanisms can have very different λ. The ratio of λ for contrail-cirrus RF to that for RF from CO_2 is the "climate efficacy" (Hansen et al. 2005) of contrail cirrus. The efficacy of contrail RF is not well known. Reported efficacy values vary from 0.3 (Rap et al. 2010a) to 0.6 (Ponater et al. 2005). The LW RF and the SW RF of contrail cirrus follow from different forcing mechanisms (LW warming in the upper troposphere, SW cooling at the surface, different diurnal cycles). It may turn out that the warming by contrails is far less than what the RF suggests.

4. Achievements, open issues, and the way forward

Since recent reviews (Heymsfield et al. 2010; Lee et al. 2010), much progress has been made in understanding contrail formation and contrail cirrus: Recent studies cover the whole lifecycle of contrails. The coupling of contrail formation processes with other climate system components has been modelled to some degree. Some first observational constraints for contrail cirrus occurrence and RF have been developed. Key parameters controlling the climate impact of contrails have been identified, as summarized in Table 1. Observation data of contrail properties compare reasonably with model results. No obvious indication for strong shattering effects has been found in past contrail measurements.

Several open issues limit progress: It is unclear why contrails are often optically thicker than expected from measured or modeled humidity. Is this an effect of underestimated ice-

supersaturation, small-scale vertical motions causing locally higher humidity, or of additional particle production? The global climate impact of contrails depends strongly on the SW/LW RF ratio. Is the uncertainty a consequence of the habit and optical properties of the ice particles or of ambient temperature and albedo of the Earth-atmosphere system? Also, future cirrus research should find out more about the ice nucleation properties of ice residuals, both from contrails and other cirrus. With respect to aerodynamic contrails, the number of ice particles surviving the wake vortex phase needs to be quantified as a prerequisite to assess its potential climate and precipitation impacts. In-situ ice particle measurements in young contrails seem to miss many of the smaller ice particles.

Further research is needed to reduce uncertainties concerning the key parameters listed in Table 1. Among others, this requires complete sets of measurements which allow constraining model variants. In-situ measurements and remote sensing from ground, aircraft, and space-instruments are to be combined with data on air traffic and weather for analysis. The contrail formation process from exhaust formation in the engine to end of the wake vortex phase needs to be investigated in more detail, in particular when discussing alternative fuels. New instruments are required to measure the small-size and small-scale cirrus properties in-situ combined with remote sensing of the ambience at contrail scales to determine local and integral contrail properties and cause-effect relationships simultaneously. Representation of ice supersaturation, temperature, wind shear, and vertical motions in NWP and climate models need to be improved. New ideas are needed to account for the complex contrail-climate interactions at scales from local contrail formation to global. The climate impact of contrail cirrus for given radiative forcing properties needs to be better quantified.

Acknowledgments. We are grateful for figures, data and comments to Darrel Baumgardner, Phil Brown, Donald Delisi, Dave Duda, Klaus Gierens, Volker Grewe, Jim Haywood, Frank

752 Holzäpfel, Nicolas Lamquin, Patrick Minnis, Christiane Voigt, Simon Unterstraßer,
753 Christiane Voigt, and Margarita Vázquez-Navarro, and three anonymous reviewers.
754

REFERENCES

Anderson, B. E., W. R. Cofer, D. R. Bagwell, J. W. Barrick, C. H. Hudgins, and K. E. Brunke, 1998: Airborne observations of aircraft aerosol emissions I: Total nonvolatile particle emission indices. *Geophys. Res. Lett.*, **25,** 1689-1692, doi:10.1029/98GL00063.

Anderson, J. D., 2010: *Fundamentals of Aerodynamics.* McGraw Hill, New Delhi.

Appleman, H., 1953: The formation of exhaust contrails by jet aircraft. *Bull. Amer. Meteorol. Soc.*, **34,** 14-20.

Atlas, D., and Z. Wang, 2010: Contrails of small and very large optical depth. *J. Atmos. Sci.*, **67,** 3065-3073, DOI: 10.1175/2010JAS3403.1.

Atlas, D., Z. Wang, and D. P. Duda, 2006: Contrails to cirrus - Morphology, microphysics, and radiative properties. *J. Appl. Meteorol. Clim.*, **45,** 5-19, doi: 10.1175/JAM2325.1.

aufm Kampe, H. J., 1943: Die Physik der Auspuffwolken hinter Flugzeugen. *Luftwissen*, **10,** 171-173, English in NASA TT-F-14047 (1971).

Bailey, M. P., and J. Hallett, 2009: A comprehensive habit diagram for atmospheric ice crystals: Confirmation from the laboratory, AIRS II, and other field studies. *J. Atmos. Sci.*, **66,** 2888-2899, DOI: 10.1175/2009JAS2883.1.

Bauer, P., A. Thorpe, and G. Brunet, 2015: The quiet revolution of numerical weather prediction. *Nature*, **525,** 47-55, doi:10.1038/nature14956.

Baum, B. A., A. J. Heymsfield, P. Yang, and S. T. Bedka, 2005: Bulk scattering properties for the remote sensing of ice clouds. Part I: Microphysical data and models. *J. Appl. Meteor.*, **44,** 1885-1895.

Baumann, R., R. Busen, H. P. Fimpel, C. Kiemle, M. Reinhardt, and M. Quante, 1993: Measurements on contrails of commercial aircraft. *Preprints of the Eighth Symposium on Meteorological Observations and Instrumentation*, AMS, Ed., 484-489.

Baumgardner, D., and W. A. Cooper, 1994: Airborne measurements in jet contrails: Characterization of the microphysical properties of aircraft wakes and exhausts. *Impact of Emissions from Aircraft and Spacecraft upon the Atmosphere*, U. Schumann, and D. Wurzel, Eds., Cologne, DLR, Mitt. 94-06, 418-423

Bedka, S. T., P. Minnis, D. P. Duda, T. L. Chee, and R. Palikonda, 2013: Properties of linear contrails in the Northern Hemisphere derived from 2006 Aqua MODIS observations. *Geophys. Res. Lett.*, **40,** 772-777, doi:10.1029/2012GL054363.

783 Birner, T., A. Dörnbrack, and U. Schumann, 2002: How sharp is the tropopause at midlatitudes? *Geophys. Res.*
784 *Lett.*, **29,** 45-41 - 45-44, doi: 10.1029/2002gl015142.
785 Bock, L., and U. Burkhardt, 2016: The temporal evolution of a long-lived contrail cirrus cluster: Simulations with
786 a global climate model. *J. Geophys. Res.*, **121,** 3548-3565, DOI: 10.1002/2015JD024475.
787 Boies, A. M., et al., 2015: Particle emission characteristics of a gas turbine with a double annular combustor.
788 Aerosol Sci. Technol. 49, . *Aerosol Sci. Techn.*, **49,** 842-855, doi:10.1080/02786826.2015.1078452.
789 Bond, T. C., et al., 2013: Bounding the role of black carbon in the climate system: A scientific assessment. *J.*
790 *Geophys. Res.*, **118,** 5380–5552, doi: 10.1002/jgrd.50171.
791 Boucher, O., et al., 2013: Clouds and Aerosols. *Climate Change 2013: The Physical Science Basis. Contribution of*
792 *Working Group I to the Fifth Assessment Report of the Intergovernmental Panel on Climate Change* T. F.
793 Stocker, and Coauthors, Eds., Cambridge University Press, 571-657
794 Brasseur, G. P., et al., 2016: Impact of aviation on climate: FAA's Aviation Climate Change Research Initiative
795 (ACCRI) Phase II. *Bull. Amer. Meteorol. Soc.*, **97,** 561-583, DOI:10.1175/BAMS-D-13-00089.1.
796 Braun-Unkhoff, M., and U. Riedel, 2015: Alternative fuels in aviation. *CEAS Aeronaut. J.*, **6,** 83–93, DOI
797 10.1007/s13272-014-0131-2.
798 Brewer, A. W., 1946: Condensation trails. *Weather*, **1,** 34-40.
799 ——, 2000: The stratospheric circulation: A personnel history. *SPARC Newsletter*, **15,** 28-32.
800 Brock, C. A., F. Schröder, B. Kärcher, A. Petzold, R. Busen, and M. Fiebig, 2000: Ultrafine particle size
801 distributions measured in aircraft exhaust plumes. *J. Geophys. Res.*, **105,** 26555-26567.
802 Burkhardt, U., and B. Kärcher, 2011: Global radiative forcing from contrail cirrus. *Nature Clim. Change*, **1,** 54-58,
803 doi: 10.1038/NCLIMATE1068.
804 Burkhardt, U., B. Kärcher, M. Ponater, K. Gierens, and A. Gettelman, 2008: Contrail cirrus supporting areas in
805 model and observations. *Geophys. Res. Lett.*, **35,** L16808, doi:10.1029/2008GL034056.
806 Busen, R., and U. Schumann, 1995: Visible contrail formation from fuels with different sulfur contents.
807 *Geophys. Res. Lett.*, **22,** 1357-1360, doi: 10.1029/95GL01312.
808 Chen, C.-C., and A. Gettelman, 2013: Simulated radiative forcing from contrails and contrail cirrus. *Atmos.*
809 *Chem. Phys.*, **13,** 12525–12536, doi:10.5194/acp-13-12525-2013.

Comstock, J. M., T. P. Ackerman, and D. D. Turner, 2004: Evidence of high ice supersaturation in cirrus clouds using ARM Raman lidar measurements. *Geophys. Res. Lett.*, **31,** L11106, doi: 10.1029/2004GL019705.

de Bruin, A., and H. Kannemans, 2004: Analysis of NLR Cessna Citation flight test data for flight test-1 in AWIATOR project. NLR, Techn. Report AW-NLR-113-010.

De Leon, R. R., M. Krämer, D. S. Lee, and J. C. Thelen, 2012: Sensitivity of radiative properties of persistent contrails to the ice water path. *Atmos. Chem. Phys.*, **12** 7893-7901.

De Visscher, I., L. Bricteux, and G. Winckelmans, 2013: Aircraft vortices in stably stratified and weakly turbulent atmospheres: Simulation and modeling. *AIAA Journal*, **51,** 551–566, doi: 10.2514/1.J051742.

Delisi, D. P., and R. E. Robins, 2000: Short-scale instabilities in trailing wake vortices in a stratified fluid. *AIAA Journal*, **38,** 1916–1923.

Delisi, D. P., and G. C. Greene, 2009: Experimental measurements of the evolution of a vortex pair in a nonstratified fluid part 1: Migration and persistence. *47th AIAA Aerospace Sciences Meeting*, AIAA, Ed., 14.

Dickson, N. C., K. M. Gierens, H. L. Rogers, and R. L. Jones, 2010: Probabilistic description of ice-supersaturated layers in low resolution profiles of relative humidity. *Atmos. Chem. Phys.*, **10,** 6749–6763.

Dietmüller, S., et al., 2016: A new radiation infrastructure for the Modular Earth Submodel System (MESSy, based on version 2.51). *Geosci. Model Dev. Discuss.*, doi:10.5194/gmd-2015-277.

Duda, D., P. Minnis, and L. Nguyen, 2001: Estimates of cloud radiative forcing in contrail clusters using GOES imagery. *J. Geophys. Res.*, **106,** 4927-4937.

Duda, D. P., and P. Minnis, 2002: Observations of aircraft dissipation trails from GOES. *Mon Wea. Rev.*, **130,** 398-406.

Duda, D. P., P. Minnis, L. Nyuyen, and R. Palikonda, 2004: A case study of the development of contrail clusters over the Great Lakes. *J. Atmos. Sci.*, **61,** 1132-1146.

Duda, D. P., P. Minnis, K. Khlopenkov, T. L. Chee, and R. Boeke, 2013: Estimation of 2006 Northern Hemisphere contrail coverage using MODIS data. *Geophys. Res. Lett.*, **40**, doi: 10.1002/grl.50097.

Duda, D. P., T. Chee, K. Khlopenkov, S. Bedka, and P. Minnis, 2015: Linear contrail coverage and cloud property retrievals from 2012 MODIS imagery over the Northern Hemisphere. *AGU Fall Meeting, San Francisco*.

836 Dyroff, C., A. Zahn, E. Christner, R. M. Forbes, A. M. Tompkins, and P. J. van Velthoven, 2015: Comparison of
837 ECMWF analysis and forecast humidity data with CARIBIC upper troposphere and lower stratosphere
838 observations. *Q. J. R. Meteorol. Soc.*, **141A,** 833–844, DOI:10.1002/qj.2400.
839 Ewald, F., L. Bugliaro, H. Mannstein, and B. Mayer, 2013: An improved cirrus detection algorithm MeCiDA2 for
840 SEVIRI and its evaluation with MODIS. *Atmos. Meas. Tech.*, **6,** 309-322, doi:10.5194/amt-6-309-2013.
841 Fahey, D. W., et al., 1995: Emission measurements of the Concorde supersonic aircraft in the lower
842 stratosphere. *Science*, **270,** 70-74.
843 Febvre, G., J. F. Gayet, A. Minikin, H. Schlager, V. Shcherbakov, O. Jourdan, R. Busen, M. Fiebig, B. Kärcher, and
844 U. Schumann, 2009: On optical and microphysical characteristics of contrails and cirrus. *J. Geophys. Res.*,
845 **114,** D02204, doi:10.1029/2008JD010184.
846 Freudenthaler, V., F. Homburg, and H. Jäger, 1995: Contrail observations by ground-based scanning lidar: Cross-
847 sectional growth. *Geophys. Res. Lett.*, **22,** 3501-3504, 10.1029/95GL03549.
848 ——, 1996: Optical parameters of contrails from lidar measurements: Linear depolarization. *Geophys. Res.*
849 *Lett.*, **23,** 3715-3718.
850 Frömming, C., M. Ponater, U. Burkhardt, A. Stenke, S. Pechtl, and R. Sausen, 2011: Sensitivity of contrail
851 coverage and contrail radiative forcing to selected key parameters. *Atmos. Env.*, **45,** 1483-1490,
852 doi:10.1016/j.atmosenv.2010.11.033.
853 Fuglestvedt, J. S., K. P. Shine, T. Berntsen, J. Cook, D. S. Lee, A. Stenke, R. B. Skeie, G. J. M. Velders, and I. A.
854 Waitz, 2010: Transport impacts on atmosphere and climate: Metrics. *Atmos. Env.*, **44,** 4648-4677,
855 doi:10.1016/j.atmosenv.2009.04.044.
856 Gao, R. C., et al., 2006: Measurements of relative humidity in a persistent contrail. *Atmos. Env.*, **40,** 1590-1600,
857 doi:10.1016/j.atmosenv.2005.11.021.
858 Gayet, J.-F., G. Febvre, G. Brogniez, H. Chepfer, W. Renger, and P. Wendling, 1996: Microphysical and optical
859 properties of cirrus and contrails. *J. Atmos. Sci.*, **53,** 126-138.
860 Gayet, J.-F., et al., 2012: The evolution of microphysical and optical properties of an A380 contrail in the vortex
861 phase. *Atmos. Chem. Phys.*, **12,** 6629-6643, doi:10.5194/acp-12-6629-2012.

862 Gerz, T., and T. Ehret, 1996: Wake dynamics and exhaust distribution behind cruising aircraft. *The*
863 *Characterization and Modification of Wakes from Lifting Vehicles in Fluids, AGARD CP 584, May 1996*, 35.31-
864 35.38.
865 Gerz, T., and F. Holzäpfel, 1999: Wing tip vortices, turbulence and the distribution of emissions. *AIAA J.*, **37,**
866 1270-1276.
867 Gettelman, A., and C. Chen, 2013: The climate impact of aviation aerosols. *Geophys. Res. Lett.*, doi:
868 10.1002/grl.50520.
869 Gierens, K., 2012: Selected topics on the interaction between cirrus clouds and embedded contrails. *Atmos.*
870 *Chem. Phys.*, **12,** 11943-11949.
871 Gierens, K., and P. Spichtinger, 2000: On the size distribution of ice-supersaturated regions in the upper
872 troposphere and lowermost stratosphere. *Ann. Geophysicae*, **18,** 499-504, doi:10.1007/s00585-000-0499-7.
873 Gierens, K., and S. Brinkop, 2012: Dynamical characteristics of ice supersaturated regions. *Atmos. Chem. Phys.*,
874 **12,** 11933-11942, doi:10.5194/acp-12-11933-2012.
875 Gierens, K., and F. Dilger, 2013: A climatology of formation conditions for aerodynamic contrails. *Atmos. Chem.*
876 *Phys. Disc.*, **13,** 14667-14693, doi: 10.5194/acpd-13-14667-2013.
877 Gierens, K., M. Kästner, and D. Klatt, 2011: Iridescent aerodynamic contrails: The Norderney case of 27 June
878 2008. *Meteorol. Z.*, **20,** 305-311, doi: 10.1127/0941-2948/2011/0497.
879 Gierens, K., P. Spichtinger, and U. Schumann, 2012: Ice supersaturation. *Atmospheric Physics - Background -*
880 *Methods - Trends*, U. Schumann, Ed., Springer, DOI: 10.1007/978-3-642-30183-4_9.
881 Gierens, K., B. Kärcher, H. Mannstein, and B. Mayer, 2009: Aerodynamic contrails: Phenomenology and flow
882 physics. *J. Atmos. Sci.*, **66,** 217-226, DOI: 10.1175/2008JAS2767.1.
883 Graf, K., U. Schumann, H. Mannstein, and B. Mayer, 2012: Aviation induced diurnal North Atlantic cirrus cover
884 cycle. *Geophys. Res. Lett.*, **39,** L16804, doi: 10.1029/2012GL052590.
885 Greene, G. C., 1986: An approximate model of wake vortex decay in the atmosphere. *J. Aircraft*, **23,** 566-573.
886 Grewe, V., T. Champougny, S. Matthes, C. Frömming, S. Brinkop, O. A. Søvde, E. A. Irvine, and L. Halscheidt,
887 2014a: Reduction of the air traffic's contribution to climate change: A REACT4C case study. *Atmos. Env.*, **94,**
888 616–625, doi:10.1016/j.atmosenv.2014.05.059.

Grewe, V., et al., 2014b: Aircraft routing with minimal climate impact: the REACT4C climate cost function modelling approach (V1.0). *Geosci. Model Dev.*, **7,** 175-201, doi:10.5194/gmd-7-175-2014.

Hansen, J., et al., 2005: Efficacy of climate forcings. *J. Geophys. Res.*, **110,** D18104, doi:10.1029/2005JD005776.

Hansen, J. E., and L. D. Travis, 1974: Light scattering in planetary atmospheres. *Space Sci. Rev.*, **16,** 527-610.

Haywood, J. M., R. P. Allan, J. Bornemann, P. M. Forster, P. N. Francis, S. Milton, G. Rädel, A. Rap, K. P. Shine, and R. Thorpe, 2009: A case study of the radiative forcing of persistent contrails evolving into contrail-induced cirrus. *J. Geophys. Res.*, **114,** D24201, doi:10.1029/2009JD012650.

Helten, M., H. G. J. Smit, D. Kley, J. Ovarlez, H. Schlager, R. Baumann, U. Schumann, P. Nedelec, and A. Marenco, 1999: In-flight comparison of MOZAIC and POLINAT water vapor measurements. *J. Geophys. Res.*, **104,** 26087-26096, doi:10.1029/1999JD900315.

Hendricks, J., B. Kärcher, and U. Lohmann, 2011: Effects of ice nuclei on cirrus clouds in a global climate model. *J. Geophys. Res.*, **116,** D18206, 10.1029/2010JD015302.

Hennemann, I., and F. Holzäpfel, 2011: Large-eddy simulation of aircraft wake vortex deformation and topology. *J. Aerosp. Eng.*, **25,** 1336-1350, doi:10.1177/0954410011402257.

Heymsfield, A., D. Baumgardner, P. DeMott, P. Forster, K. Gierens, and B. Kärcher, 2010: Contrail microphysics. *Bull. Amer. Meteorol. Soc.*, **90,** 465-472, doi: 10.1175/2009BAMS2839.1.

Heymsfield, A. J., R. P. Lawson, and G. W. Sachse, 1998: Growth of ice crystals in a precipitating contrail. *Geophys. Res. Lett.*, **25,** 1335-1338, DOI: 10.1029/98GL00189.

Heymsfield, A. J., C. Schmitt, and A. Bansemer, 2013: Ice cloud particle size distributions and pressure-dependent terminal velocities from in situ observations at temperatures from 0° to -86°C. *J. Atmos. Sci.*, **70,** 4123-4154, DOI: 10.1175/JAS-D-12-0124.1.

Heymsfield, A. J., G. Thompson, H. Morrison, A. Bansemer, R. M. Rasmussen, P. Minnis, Z. Wang, and D. Zhang, 2011: Formation and spread of aircraft-Induced holes in clouds. *Science* **333**, doi: 10.1126/science.1202851.

Holzäpfel, F., 2003: Probabilistic two-phase wake vortex decay and transport model. *J. Aircraft*, **40,** 323-331, doi:10.2514/2.3096.

——, 2014: Effects of environmental and aircraft parameters on wake vortex behavior *J. Aircraft*, **51,** 1490-1500, doi: 10.2514/1.C032366.

916 Hoshizaki, H., L. B. Anderson, R. J. Conti, N. Farlow, J. W. Meyer, T. Overcamp, K. O. Redler, and V. Watson,
917 1975: Aircraft wake microscale phenomena. *The Stratosphere perturbed by Propulsion Effluents*, A. J.
918 Grobecker, Ed., 79
919 Immler, F., R. Treffeisen, D. Engelbart, K. Krüger, and O. Schrems, 2008: Cirrus, contrails, and ice supersaturated
920 regions in high pressure systems at northern mid latitudes. *Atmos. Chem. Phys.*, **8,** 1689-1699,
921 doi:10.5194/acp-8-1689-2008.
922 IPCC, 1999: *Aviation and the Global Atmosphere.* Cambridge Univ. Press, 373 pp.
923 ——, 2013: *Climate Change 2013: The Physical Science Basis. Contribution of Working Group I to the Fifth*
924 *Assessment Report of the Intergovernmental Panel on Climate Change.* Cambridge University Press,
925 Cambridge, UK.
926 Irvine, E. A., and K. P. Shine, 2015: Ice supersaturation and the potential for contrail formation in a changing
927 climate. *Earth Syst. Dynam.*, **7,** 555–568, doi:10.5194/esd-6-555-2015.
928 Iwabuchi, H., P. Yang, K. N. Liou, and P. Minnis, 2012: Physical and optical properties of persistent contrails:
929 Climatology and interpretation. *J. Geophys. Res.*, **117,** D06215, doi:10.1029/2011JD017020.
930 Jansen, J., and A. J. Heymsfield, 2015: Microphysics of aerodynamic contrail formation processes. *J. Atmos. Sci.*,
931 **72,** 3293–3308, doi: 10.1175/JAS-D-14-0362.1.
932 Jensen, E. J., and O. B. Toon, 1997: The potential impact of soot particles from aircraft exhaust on cirrus clouds.
933 *Geophys. Res. Lett.*, **24,** 249–252, DOI: 10.1029/96GL03235.
934 Jensen, E. J., A. S. Ackermann, D. E. Stevens, O. B. Toon, and P. Minnis, 1998a: Spreading and growth of
935 contrails in a sheared environment. *J. Geophys. Res.*, **103,** 13,557-513,567, doi:10.1029/98JD02594.
936 Jensen, E. J., O. B. Toon, S. Kinne, G. W. Sachse, B. E. Anderson, K. R. Chan, C. H. Twohy, B. Gandrud, A.
937 Heymsfield, and R. C. Miake-Lye, 1998b: Environmental conditions required for contrail formation and
938 persistence. *J. Geophys. Res.*, **103,** 3929-3936, doi: 10.1029/97JD02808.
939 Jensen, E. J., O. B. Toon, S. A. Vay, J. Ovarlez, R. May, P. Bui, C. H. Twohy, B. Gandrud, R. F. Pueschel, and U.
940 Schumann, 2001: Prevalence of ice-supersaturated regions in the upper troposphere: Implications for
941 optically thin ice cloud formation. *J. Geophys. Res.*, **106,** 17253-17266, doi:10.1029/2000JD900526.

Jeßberger, P., C. Voigt, U. Schumann, I. Sölch, H. Schlager, S. Kaufmann, A. Petzold, D. Schäuble, and J.-F. Gayet, 2013: Aircraft type influence on contrail properties. *Atmos. Chem. Phys.*, **13,** 11965-11984, DOI: 10.5194/acp-13-11965-2013.

Jones, H. M., et al., 2012: A methodology for in-situ and remote sensing of microphysical and radiative properties of contrails as they evolve into cirrus. *Atmos. Chem. Phys.*, **17,** 8157-8175.

Jurkat, T., C. Voigt, F. Arnold, H. Schlager, J. Kleffmann, H. Aufmhoff, D. Schäuble, M. Schaefer, and U. Schumann, 2011: Measurements of HONO, NO, NO_y and SO_2 in aircraft exhaust plumes at cruise. *Geophys. Res. Lett.*, **38,** L10807, doi:10.1029/2011GL046884.

Kärcher, B., and F. Yu, 2009: Role of aircraft soot emissions in contrail formation. *Geophys. Res. Lett.*, **36,** L01804, doi:10.1029/2008GL036649.

Kärcher, B., and U. Burkhardt, 2013: Effects of optical depth variability on contrail radiative forcing. *Q. J. R. Meteorol. Soc.*, **139,** 1658-1664, DOI:10.1002/qj.2053.

Kärcher, B., T. Peter, U. M. Biermann, and U. Schumann, 1996: The initial composition of jet condensation trails. *J. Atmos. Sci.*, **53,** 3066-3083.

Kärcher, B., U. Burkhardt, A. Bier, L. Bock, and I. J. Ford, 2015: The microphysical pathway to contrail formation. *J. Geophys. Res.*, **120,** 7893–7927, doi: 10.1002/2015JD023491.

Kärcher, B., B. Mayer, K. Gierens, U. Burkhardt, H. Mannstein, and R. Chatterjee, 2009: Aerodynamic contrails: Microphysics and optical properties. *J. Atmos. Sci.*, **66,** 227-243, DOI: 10.1175/2008JAS2768.1.

Kaufmann, S., C. Voigt, P. Jeßberger, T. Jurkat, H. Schlager, A. Schwarzenboeck, M. Klingebiel, and T. Thornberry, 2014: In-situ measurements of ice saturation in young contrails. *Geophys. Res. Lett.*, **41,** 702-709, doi:10.1002/2013GL058276.

Khou, J.-C., W. Ghedhaifi, X. Vancassel, and F. Garnier, 2015: Spatial simulation of contrail formation in near-field of commercial aircraft. *J. Aircraft*, **52,** 1972-1983, DOI: 10.2514/1.C033101.

Khvorostyanov, V., and K. Sassen, 1998: Cloud model simulation of a contrail case study: Surface cooling against upper tropospheric warming. *Geophys. Res. Lett.*, **25,** 2145-2148.

Kienast-Sjögren, E., P. Spichtinger, and K. Gierens, 2013: Formulation and test of an ice aggregation scheme for two-moment bulk microphysics schemes. *Atmos. Chem. Phys.*, **13,** 9021-9037, doi:10.5194/acp-13-9021-2013.

970 Knollenberg, R. G., 1972: Measurements of the growth of the ice budget in a persisting contrail. *J. Atmos. Sci.*,
971 **29,** 1367-1374.
972 Koehler, K. A., P. J. DeMott, S. M. Kreidenweis, O. B. Popovicheva, M. D. Petters, C. M. Carrico, E. D. Kireeva, T.
973 D. Khokhlovac, and N. K. Shonijac, 2009: Cloud condensation nuclei and ice nucleation activity of
974 hydrophobic and hydrophilic soot particles. *Phys. Chem. Chem. Phys.*, **11** 7906–7920, DOI:
975 10.1039/b905334b.
976 Konopka, P., 1995: Analytical Gaussian solutions for anisotropic diffusion in a linear shear flow. *J. Non-Equilib.*
977 *Thermodyn.*, **20,** 78-91.
978 Korolev, A., and I. P. Mazin, 2003: Supersaturation of water vapor in clouds. *J. Atmos. Sci.*, **60,** 2957-2974.
979 Korolev, A., E. Emery, J. Strapp, S. Cober, G. Isaac, M. Wasey, and D. Marcotte, 2011: Small ice particles in
980 tropospheric clouds: Fact or artifact? Airborne icing instrumentation evaluation experiment. *Bull. Amer.*
981 *Meteorol. Soc.*, **92,** 967–973, doi: 10.1175/2010BAMS3141.1
982 Kristensson, A., J.-F. Gayet, J. Ström, and F. Auriol, 2000: In situ observations of a reduction in effective crystal
983 diameter in cirrus clouds near flight corridors. *Geophys. Res. Lett.*, **27,** 681-684, 10.1029/1999GL010934.
984 Kuhn, M., A. Petzold, D. Baumgardner, and F. Schröder, 1998: Particle composition of a young condensation
985 trail and of upper tropospheric aerosol. *Geophys. Res. Lett.*, **25,** 2679-2682.
986 Laken, B. A., E. Palla, D. R. Kniveton, C. J. R. Williams, and D. A. Kilham, 2012: Contrails developed under frontal
987 influences of the North Atlantic. *J. Geophys. Res.*, **117,** D11201.
988 Lamquin, N., C. J. Stubenrauch, K. Gierens, U. Burkhardt, and H. Smit, 2012: A global climatology of upper-
989 tropospheric ice supersaturation occurrence inferred from the Atmospheric Infrared Sounder calibrated by
990 MOZAIC. *Atmos. Chem. Phys.*, **12,** 381-405, doi:10.5194/acp-12-381-2012.
991 Lee, D. S., et al., 2010: Transport impacts on atmosphere and climate: Aviation. *Atmos. Env.*, **44,** 4678-4734,
992 doi:10.1016/j.atmosenv.2009.06.005.
993 Lewellen, D. C., 2012: Analytic solutions for evolving size distributions of spherical crystals or droplets
994 undergoing diffusional growth in different regimes. *J. Atmos. Sci.*, **69,** 417-434, DOI: 10.1175/JAS-D-11-029.1.
995 ——, 2014: Persistent contrails and contrail cirrus. Part II: Full lifetime behavior. *J. Atmos. Sci.*, **71,** 4420-4438,
996 DOI: 10.1175/JAS-D-13-0317.1.

997 Lewellen, D. C., and W. S. Lewellen, 2001: The effects of aircraft wake dynamics on contrail development. *J.*
998 *Atmos. Sci.*, **58,** 390-406.
999 Lewellen, D. C., O. Meza, and W. W. Huebsch, 2014: Persistent contrails and contrail cirrus. Part I: Large-eddy
1000 simulations from inception to demise. *J. Atmos. Sci.*, **70,** 4399-4419, DOI: 10.1175/JAS-D-13-0316.1.
1001 Liou, K. N., S. C. Ou, and G. Koenig, 1990: An investigation of the climatic effect of contrail cirrus. In: Air Traffic
1002 and the Environment – Background, Tendencies and Potential Global Atmospheric Effects. U. Schumann
1003 (Ed.), Lecture Notes in Engineering. *Springer Berlin***,** 154-169.
1004 Liu, X., J. E. Penner, S. J. Ghan, and M. Wang, 2007: Inclusion of ice microphysics in the NCAR Community
1005 Atmospheric Model version 3 (CAM3). *J. Clim.*, **20,** 4526-4547.
1006 Lohmann, U., P. Spichtinger, S. Jess, T. Peter, and H. Smit, 2008: Cirrus cloud formation and ice supersaturated
1007 regions in a global climate model. *Environ. Res. Lett.*, **3,** 045022 doi:10.1088/1748-9326/3/4/045022.
1008 Mannstein, H., R. Meyer, and P. Wendling, 1999: Operational detection of contrails from NOAA-AVHRR data.
1009 *Int. J. Remote Sensing*, **20,** 1641-1660, doi: 10.1080/014311699212650.
1010 Mannstein, H., A. Brömser, and L. Bugliaro, 2010: Ground-based observations for the validation of contrails and
1011 cirrus detection in satellite imagery. *Atmos. Meas. Tech.*, **3,** 655-669, DOI: 10.5194/amt-3-655-2010.
1012 Markowicz, K. M., and M. L. Witek, 2011: Simulations of contrail optical properties and radiative forcing for
1013 various crystal shapes. *J. Appl. Meteorol. Clim.*, **50,** 1740-1755, DOI: 10.1175/2011JAMC2618.1.
1014 Marquart, S., M. Ponater, F. Mager, and R. Sausen, 2003: Future development of contrail cover, optical depth
1015 and radiative forcing: Impacts of increasing air traffic and climate change. *J. Clim.*, **16,** 2890-2904.
1016 Mayer, B., and A. Kylling, 2005: The libRadtran software package for radiative transfer calculations: Description
1017 and examples of use. *Atmos. Chem. Phys.*, **5,** 1855–1877, doi:10.5194/acp-5-1855-2005.
1018 Meerkötter, R., U. Schumann, P. Minnis, D. R. Doelling, T. Nakajima, and Y. Tsushima, 1999: Radiative forcing by
1019 contrails. *Ann. Geophysicae*, **17,** 1080-1094, doi: 10.1007/s00585-999-1080-7.
1020 Minnis, P., J. K. Ayers, R. Palikonda, and D. Phan, 2004: Contrails, cirrus trends, and climate. *J. Clim.*, **17,** 1671-
1021 1685.
1022 Minnis, P., D. F. Young, D. P. Garber, L. Nguyen, W. L. Smith Jr., and R. Palikonda, 1998: Transformation of
1023 contrails into cirrus during SUCCESS. *Geophys. Res. Lett.*, **25,** 1157-1160, doi:10.1029/97GL03314.

1024 Minnis, P., S. T. Bedka, D. P. Duda, K. M. Bedka, T. Chee, J. K. Ayers, R. Palikonda, D. A. Spangenberg, K. V.
1025 Khlopenkov, and R. Boeke, 2013: Linear contrail and contrail cirrus properties determined from satellite
1026 data. *Geophys. Res. Lett.*, **40,** 3220-3226, doi: 10.1002/grl.50569.
1027 Minnis, P., J.K. Ayers, M.L. Nordeen and S.P. Weaver, 2003: Contrail frequency over the United States from
1028 surface observations. *J. Clim.* , **16,** 3447-3462.
1029 Misaka, T., F. Holzäpfel, and T. Gerz, 2015: Large-eddy simulation of aircraft wake evolution from roll-up until
1030 vortex decay. *AIAA J.*, **53,** 2646-2670, DOI: 10.2514/1.J053671.
1031 Misaka, T., F. Holzäpfel, I. Hennemann, T. Gerz, M. Manhart, and F. Schwertfirm, 2012: Vortex bursting and
1032 tracer transport of a counter-rotating vortex pair. *Phys. Fluids*, **24,** 025104, doi: 10.1063/1.3684990.
1033 Moore, R. H., et al., 2015: Influence of jet fuel composition on aircraft engine emissions: A synthesis of aerosol
1034 emissions data from the NASA APEX, AAFEX, and ACCESS missions. *Energy Fuels*, **29,** 2591−2600, DOI:
1035 10.1021/ef502618w.
1036 Myhre, G., et al., 2009: Intercomparison of radiative forcing calculations of stratospheric water vapour and
1037 contrails. *Meteorol. Z.*, **18,** 585-596, DOI 10.1127/0941-2948/2009/0411.
1038 Naiman, A. D., S. K. Lele, and M. Z. Jacobson, 2011: Large eddy simulations of contrail development: Sensitivity
1039 to initial and ambient conditions over first twenty minutes. *J. Geophys. Res.*, **116,** D21208,
1040 doi:10.1029/2011JD015806.
1041 Ovarlez, J., P. van Velthoven, G. Sachse, S. Vay, H. Schlager, and H. Ovarlez, 2000: Comparison of water vapor
1042 measurements from POLINAT2 with ECMWF analyses in high humidity conditions. *J. Geophys. Res.*, **105,**
1043 3737-3744.
1044 Ovarlez, J., J. F. Gayet, K. Gierens, J. Ström, H. Ovarlez, F. Auriol, R. Busen, and U. Schumann, 2002: Water vapor
1045 measurements inside cirrus clouds in northern and southern hemispheres during INCA. *Geophys. Res. Lett.*,
1046 **29,** 60-61 - 60-64, doi: 10.1029/2001gl014440.
1047 Paoli, R., and K. Shariff, 2016: Contrail modeling and simulation. *Annu. Rev. Fluid Mech.*, **48,** 393–427, doi:
1048 10.1146/annurev-fluid-010814-013619.
1049 Paoli, R., L. Nybelen, J. Picot, and D. Cariolle, 2013: Effects of jet/vortex interaction on contrail formation in
1050 supersaturated conditions. *Phys. Fluids*, **25,** 053305.

1051 Paoli, R., O. Thouron, J. Escobar, J. Picot, and D. Cariolle, 2014: High-resolution large-eddy simulations of stably
1052 stratified flows: application to subkilometer-scale turbulence in the upper troposphere–lower stratosphere.
1053 *Atmos. Chem. Phys.*, **14,** 5037-5055, doi:10.5194/acp-14-5037-2014.
1054 Peck, J., O. O. Oluwole, H.-W. Wong, and R. C. Miake-Lye, 2013: An algorithm to estimate aircraft cruise black
1055 carbon emissions for use in developing a cruise emissions inventory. *J. Air Waste Managem. Assoc.*, **63,** 367-
1056 375, doi: 10.1080/10962247.2012.751467.
1057 Pedgley, D. E., 2008: Some thoughts on fallstreak holes. *Weather*, **63,** 356-360.
1058 Penner, J. E., Y. Chen, M. Wang, and X. Liu, 2009: Possible influence of anthropogenic aerosols on cirrus clouds
1059 and anthropogenic forcing. *Atmos. Chem. Phys.*, **9,** 879-896, 10.5194/acp-9-879-2009.
1060 Petzold, A., A. Döpelheuer, C. A. Brock, and F. Schröder, 1999: In situ observation and model calculations of
1061 black carbon emission by aircraft at cruise altitude. *J. Geophys. Res.*, **104,** 22171-22181.
1062 Petzold, A., et al., 1997: Near-field measurements on contrail properties from fuels with different sulfur
1063 content. *J. Geophys. Res.*, **102,** 29867-29880, doi: 10.1029/97JD02209.
1064 Petzold, A., et al., 2013: Recommendations for reporting “black carbon” measurements. *Atmos. Chem. Phys.*,
1065 **13,** 8365–8379, doi:10.5194/acp-13-8365-2013.
1066 Picot, J., R. Paoli, O. Thouron, and D. Cariolle, 2015: Large-eddy simulation of contrail evolution in the vortex
1067 phase and its interaction with atmospheric turbulence. *Atmos. Chem. Phys.*, **15,** 7369-7389.
1068 Poellot, M. R., W. P. Arnott, and J. Hallett, 1999: In situ observations of contrail microphysics and implications
1069 for their radiative impact. *J. Geophys. Res.*, **104,** 12077-12084, DOI: 10.1029/1999JD900109.
1070 Ponater, M., S. Marquart, R. Sausen, and U. Schumann, 2005: On contrail climate sensitivity. *Geophys. Res.*
1071 *Lett.*, **32,** L10706, 10.1029/2005gl022580.
1072 Ponater, M., S. Marquart and R. Sausen, 2002: Contrails in a comprehensive global climate model:
1073 Parameterization and radiative forcing results. *J. Geophys. Res.*, **107,** 4164, 10.1029/2001JD000429.
1074 Rap, A., P. M. Forster, J. M. Haywood, A. Jones, and O. Boucher, 2010a: Estimating the climate impact of linear
1075 contrails using the UK Met Office climate model. *Geophys. Res. Lett.*, **37,** L20703,
1076 doi:10.1029/2010GL045161.

1077 Rap, A., P. M. Forster, A. Jones, O. Boucher, J. M. Haywood, N. Bellouin, and R. R. D. Leon, 2010b:
1078 Parameterization of contrails in the UK Met Office Climate Model. *J. Geophys. Res.*, **115,** D10205,
1079 doi:10.1029/2009JD012443.
1080 Rojo, C., X. Vancassel, P. Mirabel, J.-L. Ponche, and F. Garnier, 2015: Impact of alternative jet fuels on aircraft-
1081 induced aerosols. *Fuels*, **144,** 335-341, doi:10.1016/j.fuel.2014.12.021.
1082 Ryan, A. C., A. R. MacKenzie, S. Watkins, and R. Timmis, 2011: World War II contrails: a case study of aviation-
1083 induced cloudiness. *Int. J. Climatol.*, doi: 10.1002/joc.2392.
1084 Sarpkaya, T., 1983: Trailing vortices in homogeneous and density stratified media. *J. Fluid Mech.*, **136,** 85-109,
1085 doi: 10.1017/S0022112083002074.
1086 Sassen, K., 1979: Iridescence in an aircraft contrail. *J. Opt. Soc. Am.*, **69,** 1080-1083.
1087 Sausen, R., K. Gierens, M. Ponater, and U. Schumann, 1998: A diagnostic study of the global distribution of
1088 contrails. Part I: Present day climate. *Theor. Appl. Climat.*, **61,** 127 - 141, doi: 10.1007/s007040050058.
1089 Schäuble, D., et al., 2009: Airborne measurements of the nitric acid partitioning in persistent contrails. *Atmos.*
1090 *Chem. Phys.*, **9,** 8189-8197, doi:10.5194/acp-9-8189-2009.
1091 Schröder, F. P., B. Kärcher, A. Petzold, R. Baumann, R. Busen, C. Hoell, and U. Schumann, 1998: Ultrafine
1092 aerosol particles in aircraft plumes: In situ observations. *Geophys. Res. Lett.*, **25,** 2789-2792.
1093 Schröder, F. P., B. Kärcher, C. Duroure, J. Ström, A. Petzold, J.-F. Gayet, B. Strauss, P. Wendling, and S.
1094 Borrmann, 2000: The transition of contrails into cirrus clouds. *J. Atmos. Sci.*, **57,** 464-480.
1095 Schumann, U., 1996: On conditions for contrail formation from aircraft exhausts. *Meteorol. Z.*, **5,** 4-23.
1096 ——, 2002: Contrail Cirrus. *Cirrus*, D. K. Lynch, K. Sassen, D. O'C. Starr, and G. Stephens, Eds., Oxford Univ.
1097 Press, 231-255
1098 Schumann, U., 2005: Formation, properties and climate effects of contrails. *Compt. Rend. Phys.*, **6,** 549 - 565.
1099 Schumann, U., 2012: A contrail cirrus prediction model. *Geosci. Model Dev.*, **5,** 543–580, doi: 10.5194/gmd-5-
1100 543-2012.
1101 Schumann, U., and P. Wendling, 1990: Determination of contrails from satellite data and observational results.
1102 In: Air Traffic and the Environment – Background, Tendencies and Potential Global Atmospheric Effects. U.
1103 Schumann (Ed.), Lecture Notes in Engineering. *Springer Berlin*, 138-153.

1104 Schumann, U., and K. Graf, 2013: Aviation-induced cirrus and radiation changes at diurnal timescales. *J.*
1105 *Geophys. Res.*, **118,** 2404-2421, doi: 10.1002/jgrd.50184.
1106 Schumann, U., R. Busen, and M. Plohr, 2000: Experimental test of the influence of propulsion efficiency on
1107 contrail formation. *J. Aircraft*, **37,** 1083 - 1087.
1108 Schumann, U., P. Jeßberger, and C. Voigt, 2013a: Contrail ice particles in aircraft wakes and their climatic
1109 importance. *Geophys. Res. Lett.*, **40,** 2867-2872 doi: 10.1002/grl.50539.
1110 Schumann, U., K. Graf, H. Mannstein, and B. Mayer, 2012a: Contrails: Visible aviation induced climate impact.
1111 *Atmospheric Physics - Background - Methods - Trends*, U. Schumann, Ed., Springer, 239-257, DOI:
1112 10.1007/978-3-642-30183-4_15.
1113 Schumann, U., B. Mayer, K. Graf, and H. Mannstein, 2012b: A parametric radiative forcing model for contrail
1114 cirrus. *J. Appl. Meteorol. Clim.*, **51,** 1391-1406, doi: 10.1175/JAMC-D-11-0242.1.
1115 Schumann, U., J. E. Penner, Y. Chen, C. Zhou, and K. Graf, 2015: Dehydration effects from contrails in a coupled
1116 contrail-climate model. *Atmos. Chem. Phys.*, **15,** 11179-11199, doi:10.5194/acp-15-11179-2015.
1117 Schumann, U., H. Schlager, F. Arnold, R. Baumann, P. Haschberger, and O. Klemm, 1998: Dilution of aircraft
1118 exhaust plumes at cruise altitudes. *Atmos. Env.*, **32,** 3097-3103.
1119 Schumann, U., J. Ström, R. Busen, R. Baumann, K. Gierens, M. Krautstrunk, F. P. Schröder, and J. Stingl, 1996: In
1120 situ observations of particles in jet aircraft exhausts and contrails for different sulfur-containing fuels. *J.*
1121 *Geophys. Res.*, **101,** 6853-6870, doi: 10.1029/95JD03405.
1122 Schumann, U., B. Mayer, K. Gierens, S. Unterstrasser, P. Jessberger, A. Petzold, C. Voigt, and J.-F. Gayet, 2011:
1123 Effective radius of ice particles in cirrus and contrails. *J. Atmos. Sci.*, **68,** 300-321, DOI:
1124 10.1175/2010JAS3562.1.
1125 Schumann, U., R. Hempel, H. Flentje, M. Garhammer, K. Graf, S. Kox, H. Lösslein, and B. Mayer, 2013b: Contrail
1126 study with ground-based cameras. *Atmos. Meas. Tech.*, **6,** 3597-3612, doi:10.5194/amt-6-3597-2013.
1127 Schumann, U., F. Arnold, R. Busen, J. Curtius, B. Kärcher, A. Petzold, H. Schlager, F. Schröder, and K. H.
1128 Wohlfrom, 2002: Influence of fuel sulfur on the composition of aircraft exhaust plumes: The experiments
1129 SULFUR 1-7. *J. Geophys. Res.*, **107,** 4247, doi:10.1029/2001JD000813.
1130 Scorer, R. S., and L. J. Davenport, 1970: Contrails and aircraft downwash. *J. Fluid Mech.*, **43,** 451-464.

1131 Sharman, R. D., S. B. Trier, T. P. Lane, and J. D. Doyle, 2012: Sources and dynamics of turbulence in the upper
1132 troposphere and lower stratosphere: A review. *Geophys. Res. Lett.*, **39,** L12803, doi:10.1029/2012GL051996.
1133 Smit, H. G. J., S. Rohs, P. Neis, D. Boulanger, M. Krämer, A. Wahner, and A. Petzold, 2014: Reanalysis of upper
1134 troposphere humidity data from the MOZAIC programme for the period 1994 to 2009. *Atmos. Chem. Phys.*,
1135 **14,** 13241–13255, doi:10.5194/acp-14-13241-2014.
1136 Spichtinger, P., and M. Leschner, 2016: Horizontal scales of ice-supersaturated regions. *Tellus*, **B 68,** 29020, doi:
1137 10.3402/tellusb.v68.29020.
1138 Spichtinger, P., K. Gierens, and A. Dörnbrack, 2005: Formation of ice supersaturation by mesoscale gravity
1139 waves. *Atmos. Chem. Phys.*, **5,** 1243-1255, doi:10.5194/acp-5-1243-2005.
1140 Spinhirne, J. D., W. D. Hart, and D. P. Duda, 1998: Evolution of the morphology and microphysics of contrail
1141 cirrus from airborne remote sensing. *Geophys. Res. Lett.*, **25,** 1153-1156, 10.1029/97GL03477.
1142 Stettler, M. E. J., A. M. Boies, A. Petzold, and S. R. H. Barrett, 2013: Global civil aviation black carbon emissions.
1143 *Env. Sci. Techn.*, **47,** 10397-10404, DOI: 10.1021/es401356v.
1144 Stordal, F., G. Myhre, E. J. G. Stordal, W. B. Rossow, D. S. Lee, W. Arlander, and T. Svendby, 2005: Is there a
1145 trend in cirrus cloud cover due to aircraft traffic? *Atmos. Chem. Phys.*, **5,** 2155-2162, doi:10.5194/acp-5-
1146 2155-2005.
1147 Ström, J., and S. Ohlsson, 1998: In situ measurements of enhanced crystal number densities in cirrus clouds
1148 caused by aircraft exhaust. *J. Geophys. Res.*, **103,** 11355-11362, 10.1029/98JD00807.
1149 Stuber, N., M. Ponater, and R. Sausen, 2005: Why radiative forcing might fail as a predictor of climate change.
1150 *Climate Dynamics*, **24,** 497-510, doi: 10-1007/s00382-004-0497-7.
1151 Sussmann, R., 1997: Optical properties of contrail-induced cirrus: Discussion of unusual halo phenomena. *Appl.*
1152 *Opt.*, **36,** 4195-4201.
1153 Sussmann, R., and K. Gierens, 1999: Lidar and numerical studies on the different evolution of vortex pair and
1154 secondary wake in young contrails. *J. Geophys. Res.*, **104,** 2131-2142.
1155 ——, 2001: Differences in early contrail evolution of two-engine versus four-engine aircraft: Lidar
1156 measurements and numerical simulations. *J. Geophys. Res.* , **106,** 4899-4911.
1157 Thuman, W. C., and E. Robinson, 1954: Studies of Alaskan ice-fog particles. *J. Meteor.*, **11,** 151-156.

Timko, M. T., T. B. Onasch, M. J. Northway, J. T. Jayne, M. R. Canagaratna, S. C. Herndon, E. C. Wood, R. C. Miake-Lye, and W. B. Knighton, 2010: Gas turbine engine emissions - Part II: Chemical properties of particulate matter. *J. Eng. Gas Turbines Power*, **132,** 061505, doi:10.2514/1.32293.

Tompkins, A., K. Gierens, and G. Rädel, 2007: Ice supersaturation in the ECMWF Integrated Forecast System. *Q. J. R. Meteorol. Soc.*, **133,** 53–63, doi: 10.1002/qj.14.

Unterstrasser, S., 2016: Properties of young contrails – a parametrisation based on large-eddy simulations. *Atmos. Chem. Phys.*, **16,** 2059-2082, doi:10.5194/acp-16-2059-2016.

Unterstrasser, S., and K. Gierens, 2010a: Numerical simulations of contrail-to-cirrus transition - Part 2: Impact of initial ice crystal number, radiation, stratification, secondary nucleation and layer depth. *Atmos. Chem. Phys.*, **10,** 2037-2051, doi:10.5194/acp-10-2037-2010.

——, 2010b: Numerical simulations of contrail-to-cirrus transition - Part 1: An extensive parametric study. *Atmos. Chem. Phys.*, **10,** 2017-2036, doi:10.5194/acp-10-2017-2010.

Unterstrasser, S., and I. Sölch, 2012: Numerical modeling of contrail cluster formation. *Proceedings of the 3rd International Conference on Transport, Atmosphere and Climate (TAC-3)* R. Sausen, S. Unterstrasser, and A. Blum, Eds., 114-119

Unterstrasser, S., and N. Görsch, 2014: Aircraft-type dependency of contrail evolution. *J. Geophys. Res.*, **119,** 14015-14027, doi:10.1002/2014JD022642.

Unterstrasser, S., I. Sölch, and K. Gierens, 2012: Cloud resolving modeling of contrail evolution. *Atmospheric Physics - Background - Methods - Trends*, U. Schumann, Ed., Springer, 543-559, doi: 10.11007/978-3-642-30183-4_33.

Vázquez-Navarro, M., H. Mannstein, and S. Kox, 2015: Contrail life cycle and properties from 1 year of MSG/SEVIRI rapid-scan images. *Atmos. Chem. Phys.*, **15,** 8739-8749, doi:10.5194/acp-15-8739-2015.

Voigt, C., U. Schumann, P. Jessberger, T. Jurkat, A. Petzold, J.-F. Gayet, M. Krämer, T. Thornberry, and D. W. Fahey, 2011: Extinction and optical depth of contrails. *Geophys. Res. Lett.*, **38,** L11806 doi:10.1029/2011GL047189.

Voigt, C., et al., 2010: In-situ observations of young contrails – overview and selected results from the CONCERT campaign. *Atmos. Chem. Phys.*, **10,** 9039-9056, doi:10.5194/acp-10-9039-2010.

Voigt, C., et al., 2016: ML-CIRRUS - The airborne experiment on natural cirrus and contrail cirrus with the high-altitude long-range research aircraft HALO. *Bull. Amer. Meteorol. Soc.*, **online**, doi: 10.1175/BAMS-D-15-00213.1.

Weickmann, H., 1945: Formen und Bildung atmosphärischer Eiskristalle. *Beitr. Phys Atmos. (Contr. Atm. Phys.)*, **28,** 12-52.

Wong, H.-W., and R. C. Miake-Lye, 2010: Parametric studies of contrail ice particle formation in jet regime using microphysical parcel modeling. *Atmos. Chem. Phys.*, **10,** 3261-3272, doi:10.5194/acp-10-3261-2010.

Wu, Y., and O. Pauluis, 2015: What Is the representation of the moisture–tropopause relationship in CMIP5 Models? *J. Clim.*, **28,** 4877-4889, DOI: 10.1175/JCLI-D-14-00543.1.

Xie, Y., P. Yang, K.-N. Liou, P. Minnis, D. P. Duda, and 2012: Parameterization of contrail radiative properties for climate studies. *Geophys. Res. Lett.*, **39,** L00F02, DOI: 10.1029/2012GL054043.

Yang, P., K. N. Liou, L. Bi, C. Liu, B. Q. Yi, and B. A. Baum, 2015: On the radiative properties of ice clouds: Light scattering, remote sensing, and radiation parameterization. *Adv. Atmos. Sci.*, **32,** 32–63, doi: 10.1007/s00376-014-0011-z.

Zhou, C., and J. E. Penner, 2014: Aircraft soot indirect effect on large-scale cirrus clouds: Is the indirect forcing by aircraft soot positive or negative? *J. Geophys. Res.*, **119,** 11303-11320, DOI: 10.1002/2014JD021914.

Table 1. Key parameters controlling contrail properties and effects

Number of ice particles in young contrails, N_{ice}	Contrail lifetime, age	Climate impact
Emissions, wake dynamics	Initial number of ice particles	Total extinction and lifetime
Number of soot particles	Ambient RHi, T, p, D_{IS}	Temperature
Ambient RHi, p, Temperature	Mixing and sedimentation	Solar and terrestrial top of the atmosphere radiances
Particle losses in sinking wake vortex	Ambient vertical motion	Efficacy

List of symbols

Symbol	Description	Unit
A_i, A_c	Area of an ice particle and contrail cross-section	m^2
b_0	Wake vortex scale	m
c_p	Specific heat capacity of air at constant pressure	J kg^{-1} K^{-1}
C	r_{vol}/r_{eff}	1
D, D_c, D_w, D_{IS}	Depth, contrail depth, wake depth, ice saturation layer depth	m
D_{H2O}	Diffusivity of vapor in air	m^2 s^{-1}
EA	Total extinction per flight distance	m
EF	Energy forcing, $\int_{lifetime}$ W RF' dt	J m^{-1}
EI, EI_{H2O}, EI_{soot}	Mass emission index, of water and soot	kg kg^{-1}
f_c, f_s	Fraction of ice-forming soot particles, and of ice particles surviving the wake vortex phase	1
F	Aircraft engine thrust	N
g	Gravity	m s^{-2}
G	Slope of mixing line	Pa K^{-1}
I	Total ice mass per contrail length	kg m^{-1}
IWC	Ice water content	kg m^{-3}
m_i, m_{soot}	mass of an ice particle, soot particles	kg
m_F	Fuel consumption per flight distance	kg m^{-1}
M	Aircraft mass	kg
M_{air}, M_{H2O}	Molar mass of air and water molecules	kg mol^{-1}
N_{BV}	Brunt-Väisälä frequency	s^{-1}
N_{BV}^*	N_{BV} t_0, stratification parameter	1
N_{dil}	Dilution ratio (plume mass per burned fuel mass)	1

n_{ice}	Ice particle concentration	m^{-3}
N_{ice}	Total ice particle number per contrail length	m^{-1}
p, p_{ice}, p_{sat}	Pressure, ice saturation pressure, liquid saturation pressure	Pa
PEI, PEI_{ice}, PEI_{soot}	Particle number emission index, apparent PEI for ice, PEI for soot	kg^{-1}
Q	Fuel combustion heat	$J\ kg^{-1}$
Q_{ext}	Extinction efficiency	1
r_{area}, r_{eff}, r_{vol}	Area, effective, volume mean radius	m
RF, RF_{LW}, RF_{SW}	Radiative forcing, longwave RF and shortwave RF	$W\ m^{-2}$
RF'	Local RF	$W\ m^{-2}$
RH, RHi	Relative humidity for liquid and ice saturation	1
s	Wing span	m
SS	Ice particle surface area time integral, $\int_{lifetime} N_{ice}\ \pi\ r_{area}^2\ dt$	m s
t	Time	s
T	Temperature	K
V	Aircraft air speed	$m\ s^{-1}$
w_0	Wake vortex velocity scale	$m\ s^{-1}$
W	Contrail width	m
ε_t	Turbulent kinetic energy dissipation rate	$m^2\ s^{-3}$
ε_t^*	Non-dimensional dissipation rate	1
η	Overall propulsion efficiency	1
Γ_0	Initial wake vortex circulation	$m^2\ s^{-1}$
λ	Surface temperature climate sensitivity	$K\ W^{-1}\ m^2$
ρ, ρ_{ice}	Air density, ice bulk density	$kg\ m^{-3}$
τ	Optical depth (at solar wavelengths)	1

Figure captions

Figure 1. Contrail types. a) Exhaust contrail (photo by Josef P. Williams (Unterstrasser et al. 2012)). b) Aerodynamic contrail (photo by Dieter Klatt (Gierens et al. 2011)). c) Aircraft-induced lines and holes in supercooled liquid clouds (cloud top temperatures -35°C to -25°C); section of image with blue border lines, near North-West corner of Texas (29 January 2007, NASA, Jeff Schmaltz, MODIS Rapid Response Team). d) Contrail visible shortly behind B747-400 engines, 38000 ft, -61°C, 28 May 2004, photo by Robert Falk. e) "Soot cirrus" observed at DLR, Oberpfaffenhofen, 9:05 UTC 3 Nov 2013. f) Persistent contrails west of lake Ammersee, Germany, photo by Ch. Koenig, DLR, 23 June 2002. g) Persistent contrails and contrail cirrus, a false color NOAA-12 AVHRR image, 5 April 1995, processed by DLR.

Figure 2. a) Contrail formation principle (for G=1.65 Pa/K), identifying the points LM (maximum liquid saturation), L1 (first liquid saturation) and L2 (last liquid saturation) for given environment (E, T_E= 220 K, RHi= 1.1) and SAC threshold conditions (LC). Probability density functions of persistent contrail formation thermodynamics for 2006 air traffic from the ACCRI project and NWP data from ECMWF: b) overall-propulsion efficiency η, c) pressure; d) threshold temperature difference above ambience, e) relative humidity RHi over ice and potential RH_{LM} over liquid saturation at LM without phase changes, f) temperature at L1, LM, L2, and E (colors as in panel a).

Figure 3. Mean contrail properties versus age. a) Ice number concentration, b) ice water content, c) volume mean radius, d) optical depth, e) contrail width, f) geometrical depth, from in-situ measurements (red) (Knollenberg 1972; Baumgardner and Cooper 1994; Poellot et al. 1999; Schröder et al. 2000; Gao et al. 2006; Febvre et al. 2009; Heymsfield et al. 2010; Voigt et al. 2011; Jones et al. 2012; Jeßberger et al. 2013; Schumann et al. 2013a; Kaufmann et al.

2014) and remote sensing observations (blue) (Hoshizaki et al. 1975; Baumann et al. 1993; Freudenthaler et al. 1995, 1996; Minnis et al. 1998; Spinhirne et al. 1998; Sussmann and Gierens 1999; Duda et al. 2004; Atlas et al. 2006; Atlas and Wang 2010; Schumann et al. 2013b) and from CoCiP model simulations (shaded regions with white lines for minimum, 10%, 50%, 90%, and maximum percentiles (Schumann et al. 2015)). The cyan curves in panel d) show corresponding percentiles of optical depth data from ACTA (Vázquez-Navarro et al. 2015).

Figure 4. Maximum wake vortex sinking distance or contrail depth D versus Brunt-Väisälä frequency N_{BV}, normalized with wake vortex scales. Adapted from Schumann (2012) with additions. The red, blue, and black lines depict a parameterization for fixed dissipation $\varepsilon_t^* =$ 0.01, 0.05, and 0.23, respectively (Holzäpfel 2003). The value of ε_t^* is given in the legend when known. Filled symbols are for wake vortex descent from LES (Delisi and Robins 2000; Hennemann and Holzäpfel 2011; Misaka et al. 2012; De Visscher et al. 2013; Picot et al. 2015), tank experiments (Sarpkaya 1983; Delisi and Robins 2000; Delisi and Greene 2009), and field experiments (AWIATOR) (de Bruin and Kannemans 2004). The one-sided error bars for $N_{BV}=0$ indicate that vortex rings may descend even further in quiet air. Open symbols are contrail depth values D from observations (CONCERT (Jeßberger et al. 2013), 1-2 min ages) and LES (Lewellen et al. 2014; Unterstrasser and Görsch 2014; Picot et al. 2015) for 4-6 min ages. Single letters in the legend identify author initials.

Figure 5. Cumulative probability distribution of optical depth of contrail cirrus from simulations and observations. Adapted from Grewe et al. (2014b) with additions: G: (Grewe et al. 2014b), F: (Frömming et al. 2011), K: (Kärcher and Burkhardt 2013), Vo: (Voigt et al. 2011), I: (Iwabuchi et al. 2012), Va: (Vázquez-Navarro et al. 2015), S: (Schumann et al. 2015), D: (Duda et al. 2015).

Figure 6. Probability density functions of ages of contrails in simulations (CoCiP-CAM) and in satellite observations (ACTA). Data from Schumann et al. (2015) and Vázquez-Navarro et al. (2015).

Figure 7. Probability density functions of local longwave (LW, black) and shortwave (SW, red) local radiative forcing values (RF') of contrails derived from satellite observations (open symbols, ACTA) (Vázquez-Navarro et al. 2015) and a coupled contrail/climate model simulation (closed symbols) (Schumann et al. 2015).

Figure 8. The development of the extinction of a contrail cluster consisting initially of 8 individual contrails with time (top: 1 h, bottom: 2 h). Adapted from Unterstrasser and Sölch (2012).

Figure 9. Evolution of contrail cirrus from a spiral flight. Contrail cirrus is identified by bright white areas with low infrared (10.8 μm) brightness temperature. The satellite scenes are from NOAA AVHRR for 3 UTC times: 10:06 (age ≈ 1 h), 12:02 (≈ 3 h), 15:26 (≈ 6.5 h), from left to right. Adapted from Haywood et al. (2009).

Figure 10. Zonal means of ice supersaturation occurrence frequencies (%) from a) ECMWF, b) ECHAM, and c) AIRS, and d) frequency of high cloud occurrence from CALIOP. The lines depict the zonal mean tropopause, as computed from the AIRS data, in all panels. Adapted from Lamquin et al. (2012).

Figure 11. Global mean diurnal cycle of air traffic density, contrail cirrus coverage, and LW, SW and net RF versus local time, as derived from model simulation results (Schumann et al. 2015).

Figure 12. Left: Cirrus coverage (for τ>0.1) in a North Atlantic region, shortly before (0:00 UTC) and after (4:45 UTC) passage of a large number of airliners from North America to Europe (Graf et al. 2012). Right: Diurnal cycle of cirrus coverage (top) and LW RF (bottom) in the North Atlantic region versus time of day as derived from METEOSAT observations, for 8 individual years (thin lines) and in the 8-year mean (thick lines), and as modeled with CoCiP (thick dash-dotted). The red line shows the diurnal cycle of air traffic density (ATD). Adapted from Schumann and Graf (2013).

Figure 13. Global mean radiative forcing RF from contrail cirrus (LW: longwave; SW: shortwave; dehydration (deh.): from humidity changes in the background atmosphere; net: sum. Results from three global model studies: a) Burkhardt and Kärcher (2011), b) Schumann and Graf (2013), c) Schumann et al. (2015).

Figure 1. Contrail types. a) Exhaust contrail (photo by Josef P. Williams (Unterstrasser et al. 2012)). b) Aerodynamic contrail (photo by Dieter Klatt (Gierens et al. 2011)). c) Aircraft-induced lines and holes in supercooled liquid clouds (cloud top temperatures -35°C to -25°C); section of image with blue border lines, near North-West corner of Texas (29 January 2007, NASA, Jeff Schmaltz, MODIS Rapid Response Team). d) Contrail visible shortly behind B747-400 engines, 38000 ft, -61°C, 28 May 2004, photo by Robert Falk. e) "Soot cirrus" observed at DLR, Oberpfaffenhofen, 9:05 UTC 3 Nov 2013. f) Persistent contrails west of lake Ammersee, Germany, photo by Ch. Koenig, DLR, 23 June 2002. g) Persistent contrails and contrail cirrus, a false color NOAA-12 AVHRR image, 5 April 1995, processed by DLR.

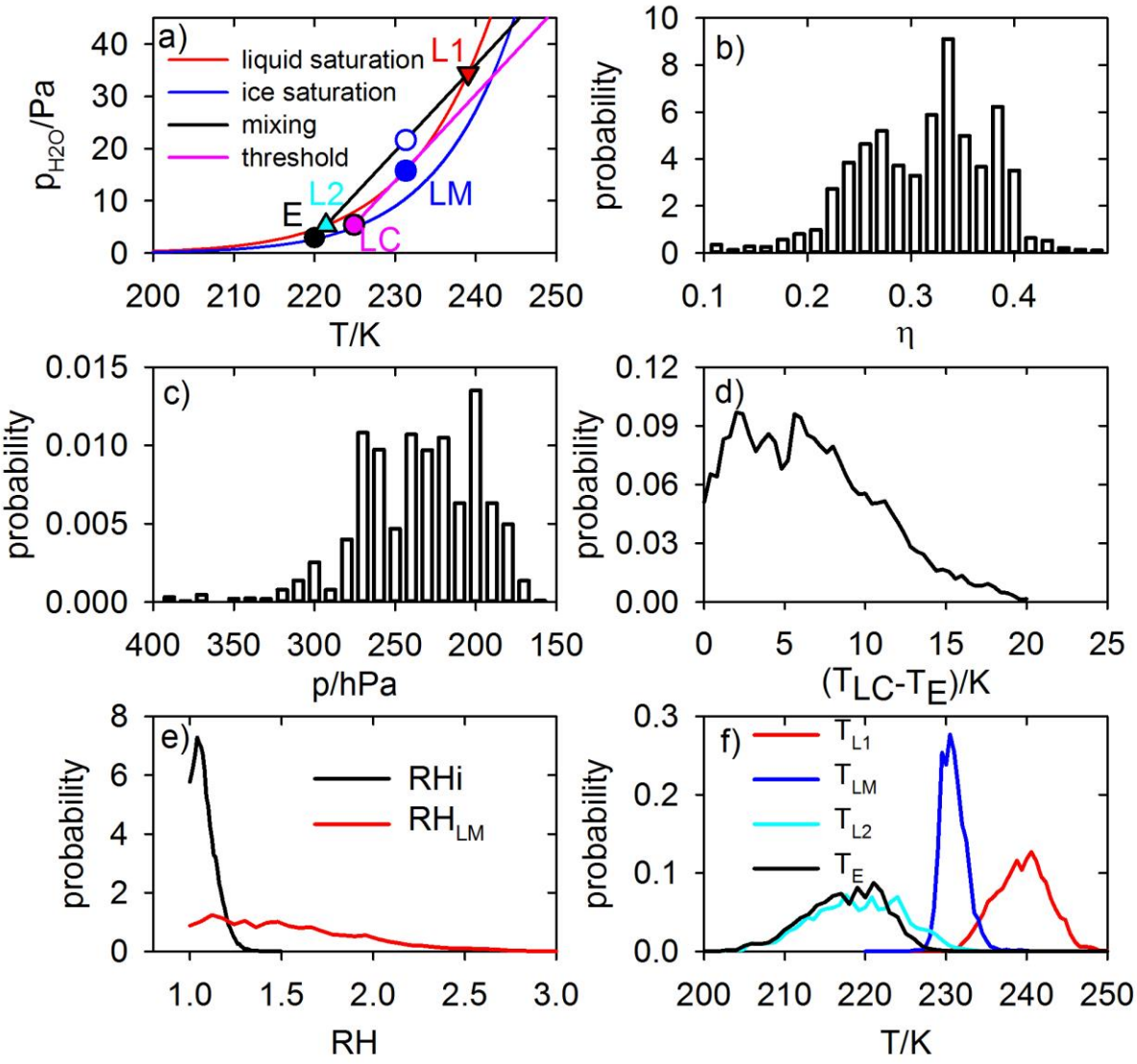

Figure 2. a) Contrail formation principle (for G=1.65 Pa/K), identifying the points LM (maximum liquid saturation), L1 (first liquid saturation) and L2 (last liquid saturation) for given environment (E, T_E= 220 K, RHi= 1.1) and SAC threshold conditions (LC). Probability density functions of persistent contrail formation thermodynamics for 2006 air traffic from the ACCRI project and NWP data from ECMWF: b) overall-propulsion efficiency η, c) pressure; d) threshold temperature difference above ambience, e) relative humidity RHi over ice and potential RH_{LM} over liquid saturation at LM without phase changes, f) temperature at L1, LM, L2, and E (colors as in panel a).

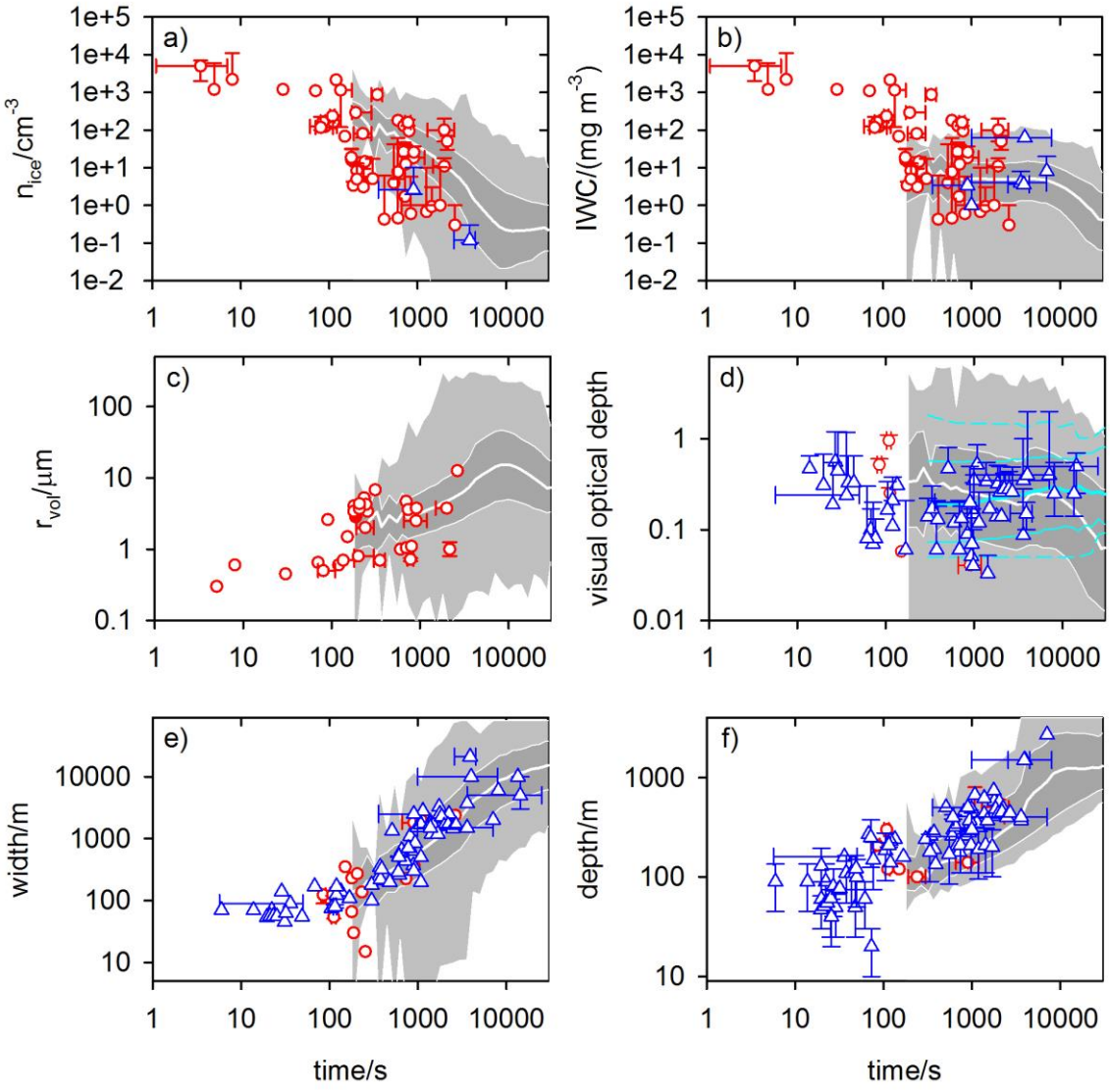

Figure 3. Mean contrail properties versus age. a) Ice number concentration, b) ice water content, c) volume mean radius, d) optical depth, e) contrail width, f) geometrical depth, from in-situ measurements (red) (Knollenberg 1972; Baumgardner and Cooper 1994; Poellot et al. 1999; Schröder et al. 2000; Gao et al. 2006; Febvre et al. 2009; Heymsfield et al. 2010; Voigt et al. 2011; Jones et al. 2012; Jeßberger et al. 2013; Schumann et al. 2013a; Kaufmann et al. 2014) and remote sensing observations (blue) (Hoshizaki et al. 1975; Baumann et al. 1993; Freudenthaler et al. 1995, 1996; Minnis et al. 1998; Spinhirne et al. 1998; Sussmann and Gierens 1999; Duda et al. 2004; Atlas et al. 2006; Atlas and Wang 2010; Schumann et al. 2013b) and from CoCiP model simulations (shaded regions with white lines for minimum, 10%, 50%, 90%, and maximum percentiles (Schumann et al. 2015)). The cyan curves in panel d) show corresponding percentiles of optical depth data from ACTA (Vázquez-Navarro et al. 2015).

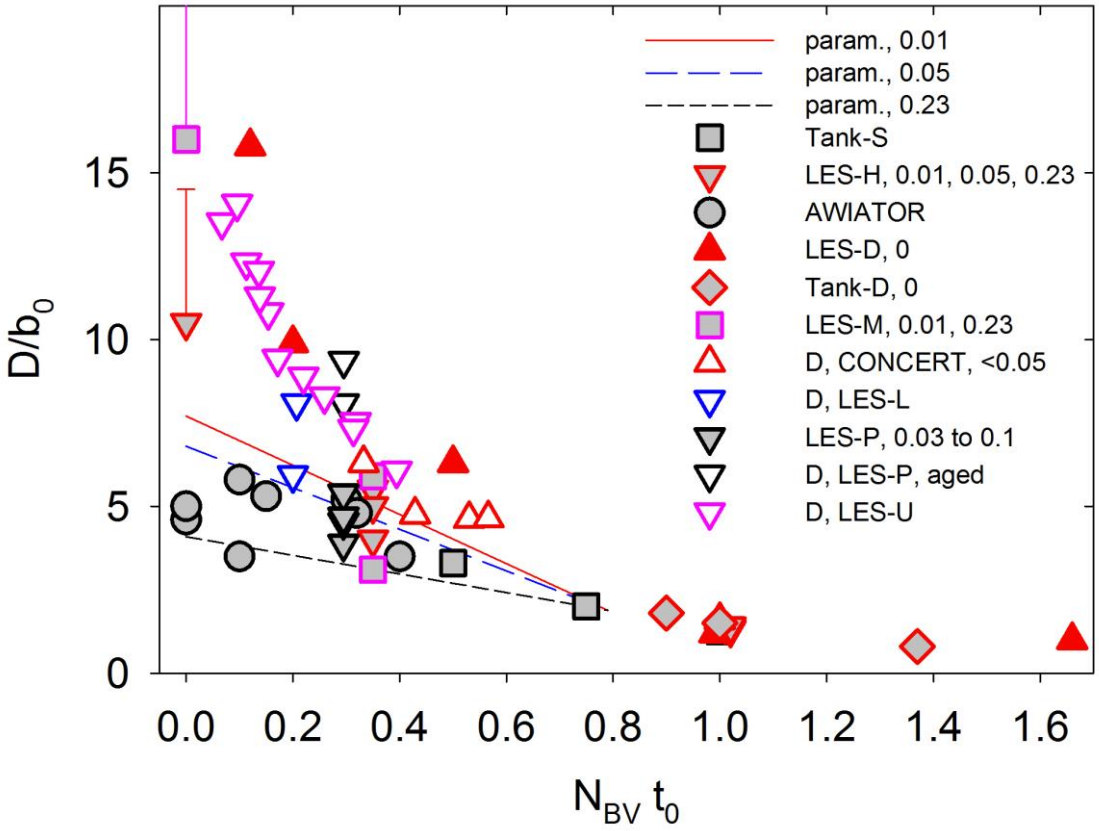

Figure 4. Maximum wake vortex sinking distance or contrail depth D versus Brunt-Väisälä frequency N_{BV}, normalized with wake vortex scales. Adapted from Schumann (2012) with additions. The red, blue, and black lines depict a parameterization for fixed dissipation $\varepsilon_t^* =$ 0.01, 0.05, and 0.23, respectively (Holzäpfel 2003). The value of ε_t^* is given in the legend when known. Filled symbols are for wake vortex descent from LES (Delisi and Robins 2000; Hennemann and Holzäpfel 2011; Misaka et al. 2012; De Visscher et al. 2013; Picot et al. 2015), tank experiments (Sarpkaya 1983; Delisi and Robins 2000; Delisi and Greene 2009), and field experiments (AWIATOR) (de Bruin and Kannemans 2004). The one-sided error bars for $N_{BV}=0$ indicate that vortex rings may descend even further in quiet air. Open symbols are contrail depth values D from observations (CONCERT (Jeßberger et al. 2013), 1-2 min ages) and LES (Lewellen et al. 2014; Unterstrasser and Görsch 2014; Picot et al. 2015) for 4-6 min ages. Single letters in the legend identify author initials.

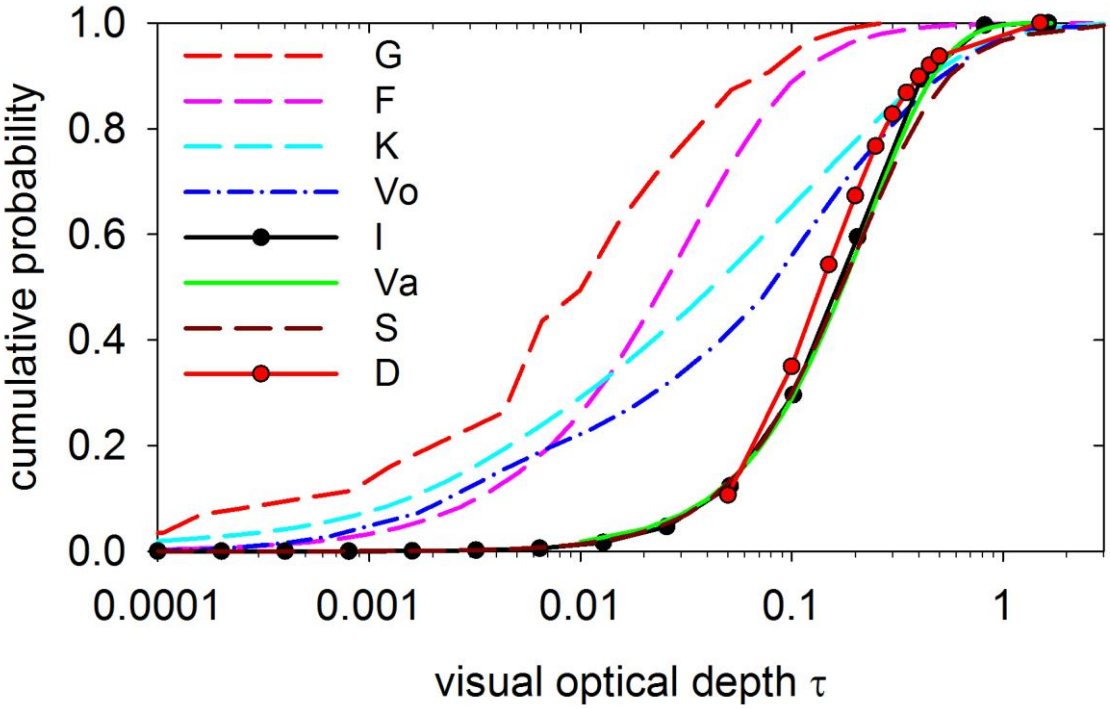

Figure 5. Cumulative probability distribution of optical depth of contrail cirrus from simulations and observations. Adapted from Grewe et al. (2014b) with additions: G: (Grewe et al. 2014b), F: (Frömming et al. 2011), K: (Kärcher and Burkhardt 2013), Vo: (Voigt et al. 2011), I: (Iwabuchi et al. 2012), Va: (Vázquez-Navarro et al. 2015), S: (Schumann et al. 2015), D: (Duda et al. 2015)..

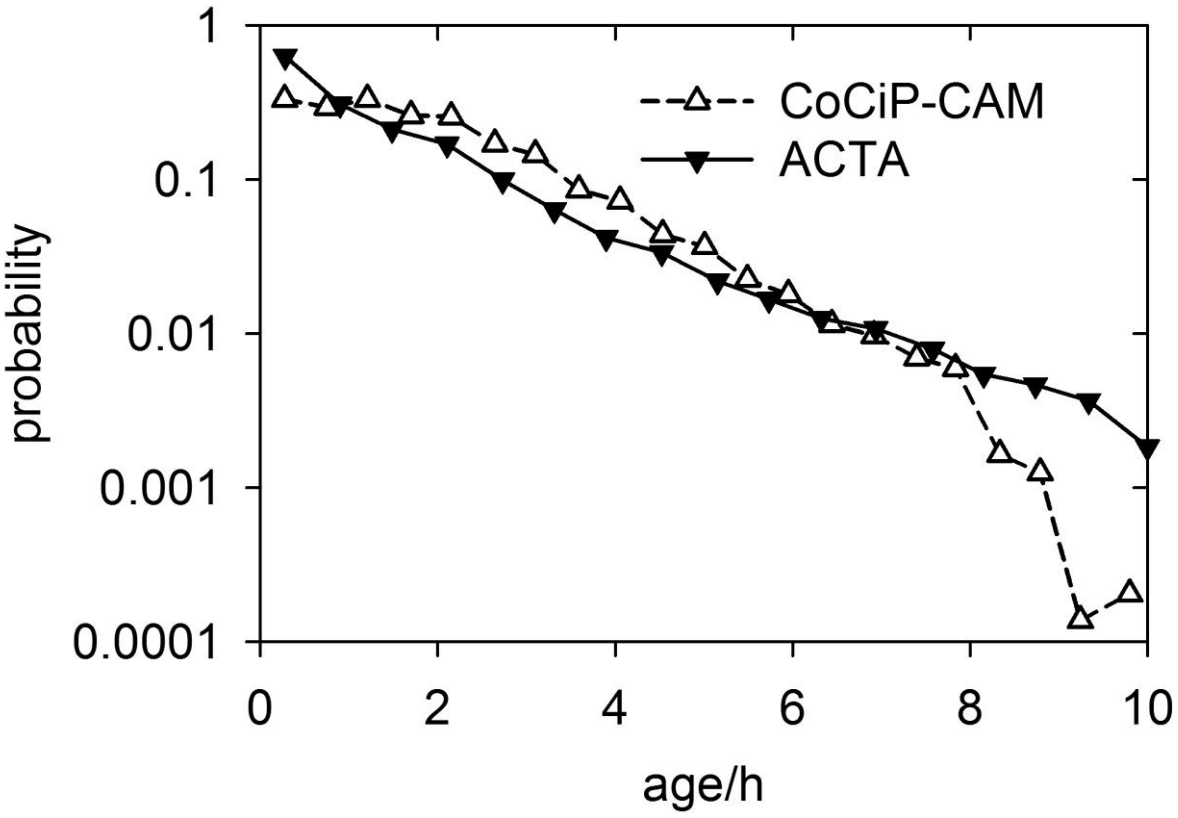

Figure 6. Probability density functions of ages of contrails in simulations (CoCiP-CAM) and in satellite observations (ACTA). Data from Schumann et al. (2015) and Vázquez-Navarro et al. (2015).

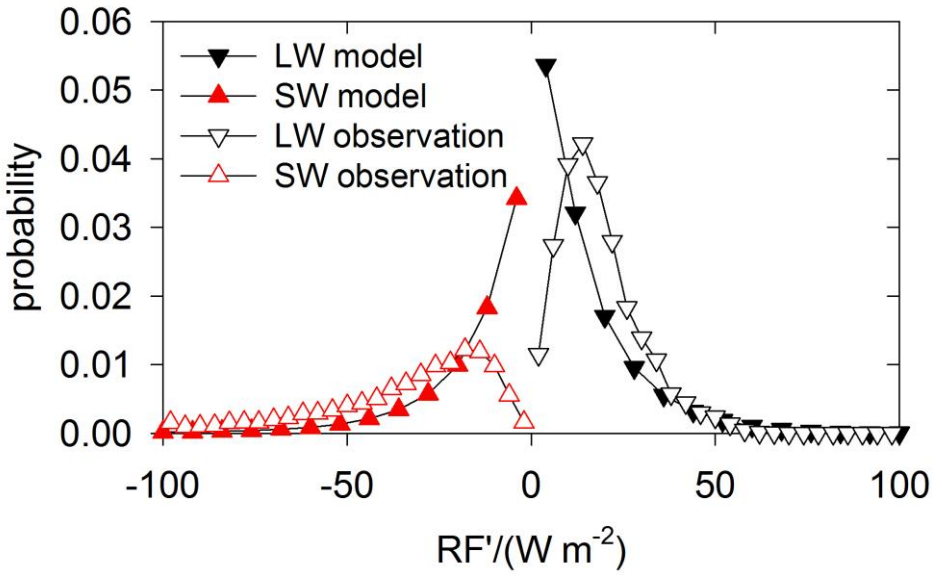

Figure 7. Probability density functions of local longwave (LW, black) and shortwave (SW, red) local radiative forcing values (RF') of contrails derived from satellite observations (open symbols, ACTA) (Vázquez-Navarro et al. 2015) and a coupled contrail/climate model simulation (closed symbols) (Schumann et al. 2015).

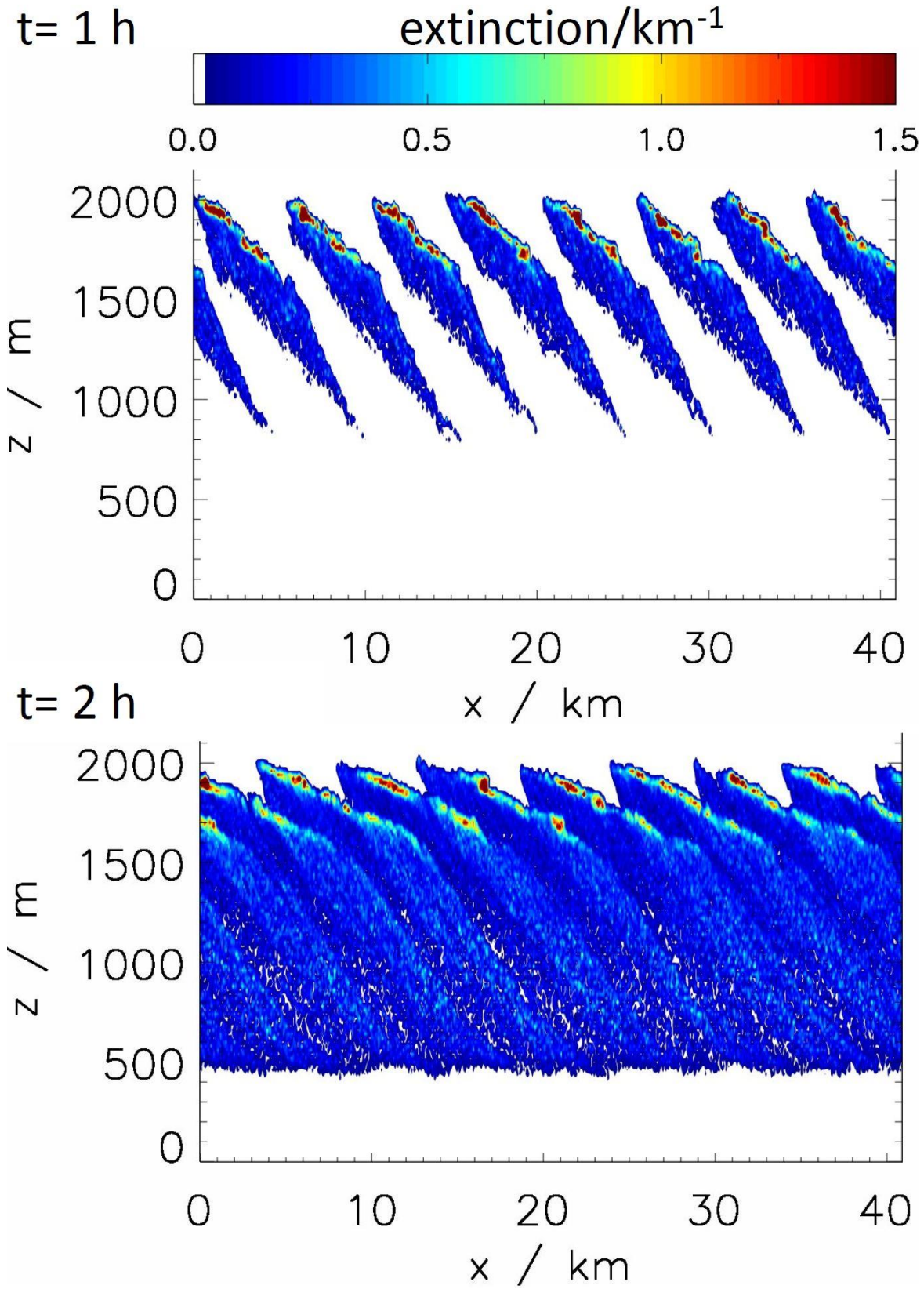

Figure 8. The development of the extinction of a contrail cluster consisting initially of 8 individual contrails with time (top: 1 h, bottom: 2 h). Adapted from Unterstrasser and Sölch (2012).

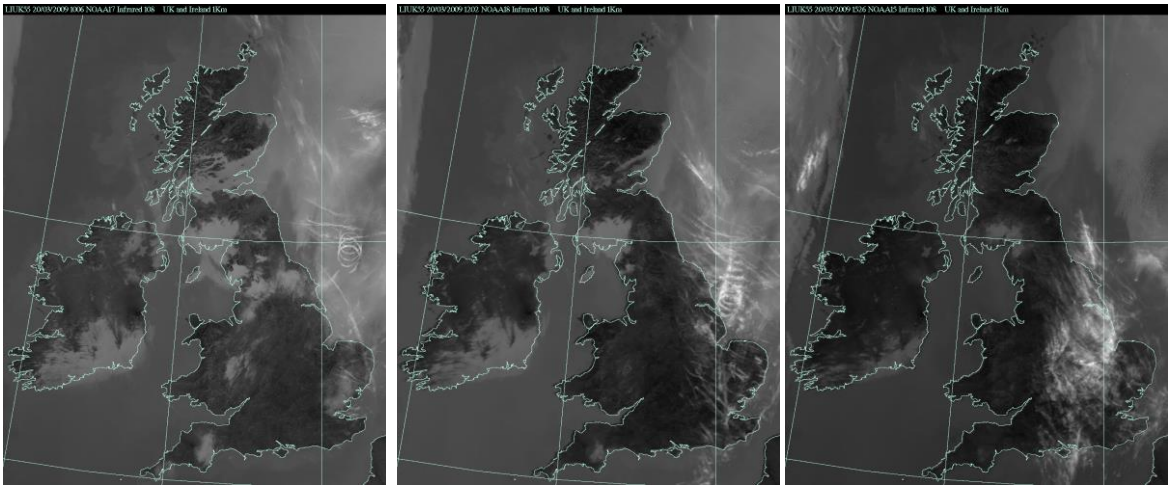

Figure 9. Evolution of contrail cirrus from a spiral flight. Contrail cirrus is identified by bright white areas with low infrared (10.8 μm) brightness temperature. The satellite scenes are from NOAA AVHRR for 3 UTC times: 10:06 (age ≈ 1 h), 12:02 (≈ 3 h), 15:26 (≈ 6.5 h), from left to right. Adapted from Haywood et al. (2009).

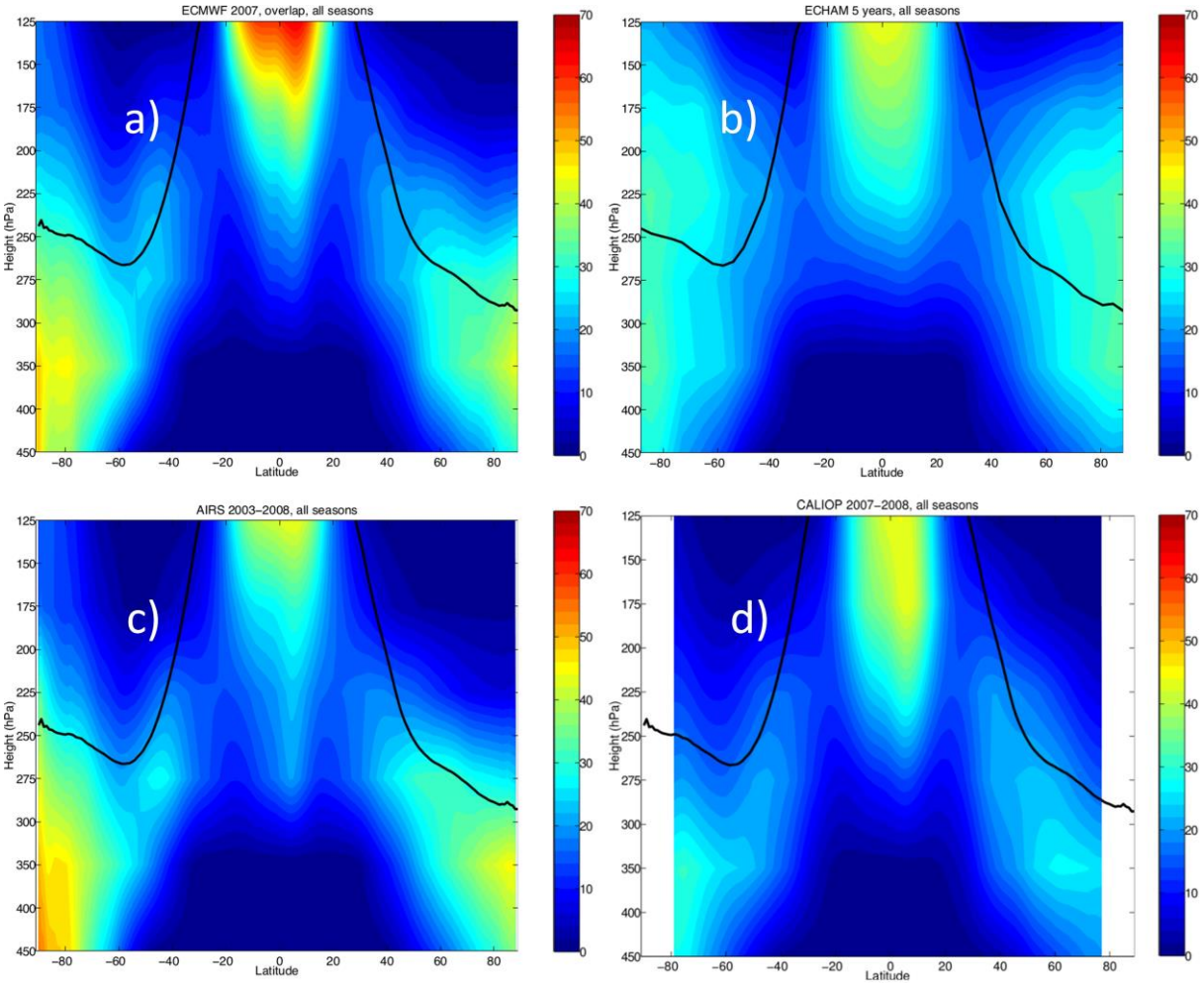

Figure 10. Zonal means of ice supersaturation occurrence frequencies (%) from a) ECMWF, b) ECHAM, and c) AIRS, and d) frequency of high cloud occurrence from CALIOP. The lines depict the zonal mean tropopause, as computed from the AIRS data, in all panels. Adapted from Lamquin et al. (2012).

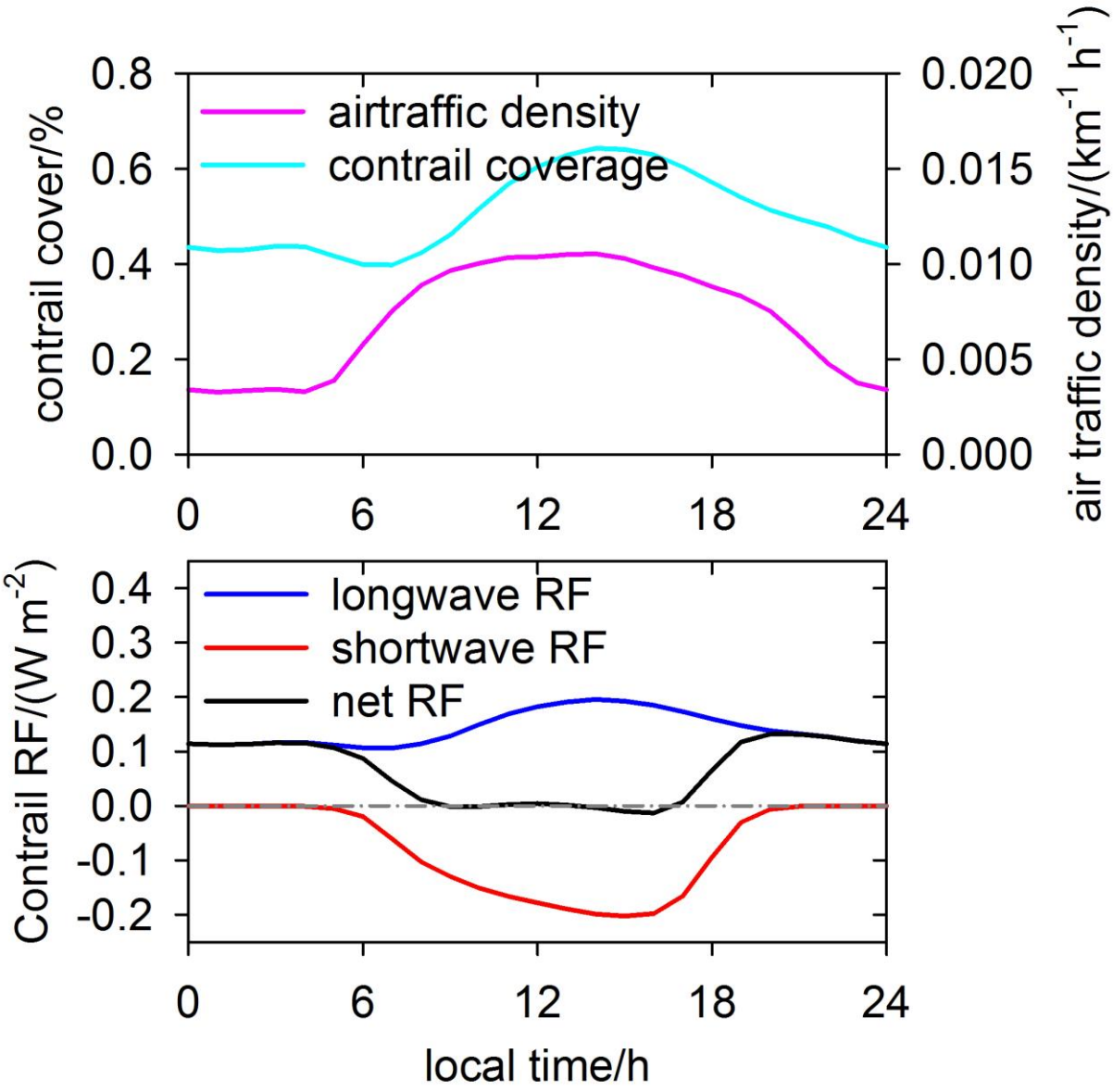

Figure 11. Global mean diurnal cycle of air traffic density, contrail cirrus coverage, and LW, SW and net RF versus local time, as derived from model simulation results (Schumann et al. 2015).

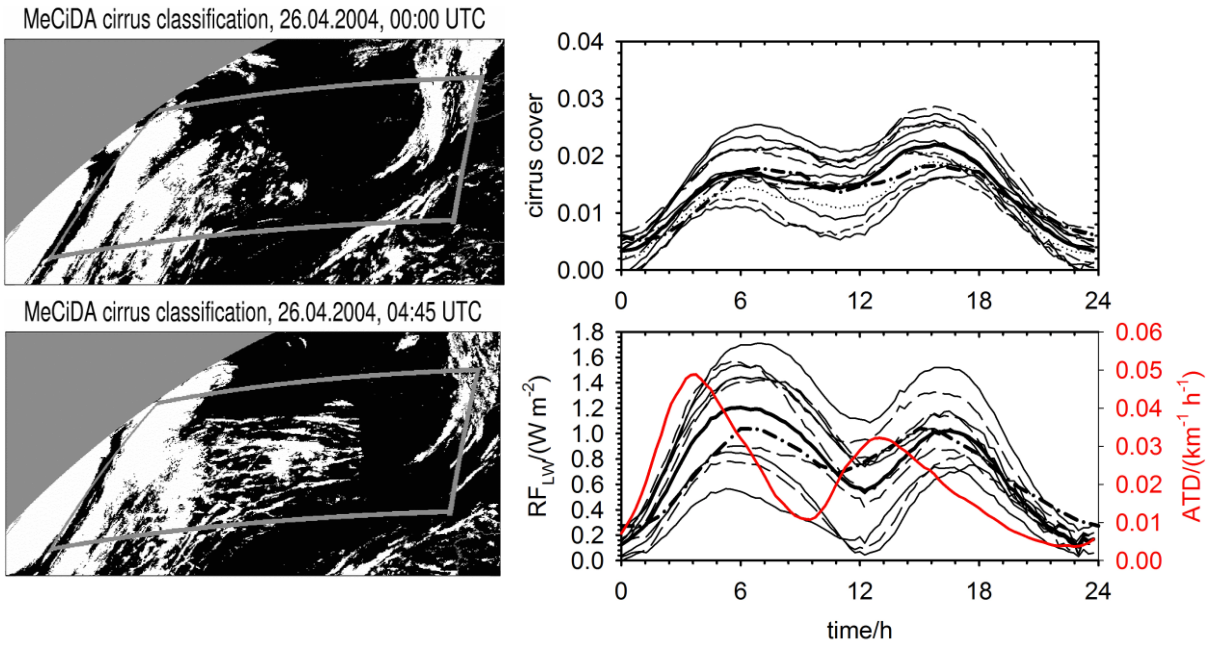

Figure 12. Left: Cirrus coverage (for τ>0.1) in a North Atlantic region, shortly before (0:00 UTC) and after (4:45 UTC) passage of a large number of airliners from North America to Europe (Graf et al. 2012). Right: Diurnal cycle of cirrus coverage (top) and LW RF (bottom) in the North Atlantic region versus time of day as derived from METEOSAT observations, for 8 individual years (thin lines) and in the 8-year mean (thick lines), and as modeled with CoCiP (thick dash-dotted). The red line shows the diurnal cycle of air traffic density (ATD). Adapted from Schumann and Graf (2013).

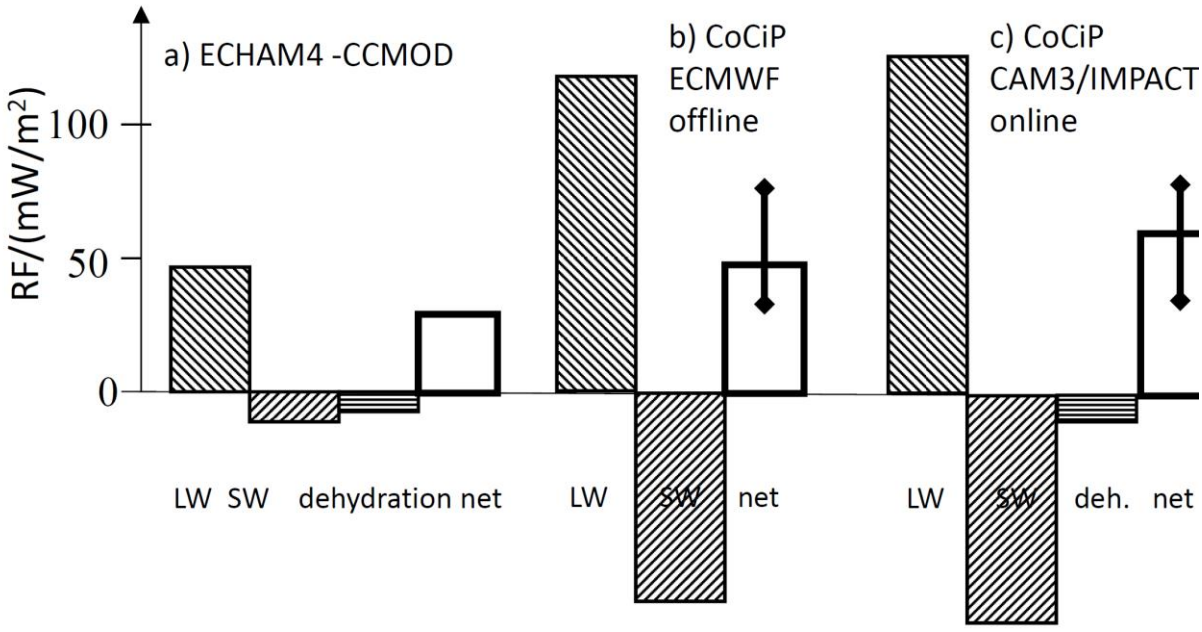

Figure 13. Global mean radiative forcing RF from contrail cirrus (LW: longwave; SW: shortwave; dehydration (deh.): from humidity changes in the background atmosphere; net: sum. Results from three global model studies: a) Burkhardt and Kärcher (2011), b) Schumann and Graf (2013), c) Schumann et al. (2015).